Ground-generation airborne wind energy design space exploration

Markus Sommerfeld[1], Martin Dörenkämper[2], Jochem De Schutter[3], and Curran Crawford[1]

[1]Institute for Integrated Energy Systems, University of Victoria, British Columbia, Canada
[2]Fraunhofer Institute for Wind Energy Systems, Oldenburg, Germany
[3]Systems Control and Optimization Laboratory IMTEK, Freiburg, Germany

Correspondence: Markus Sommerfeld (msommerf@uvic.ca)

Abstract.

While some Airborne Wind Energy System (AWES) companies aim at small-scale, temporary or remote off-grid markets, others aim to integrate utility-scale, multi-megawatt AWES into the electricity grid. This study investigates the scaling effects of single-wing, ground-generation AWESs from small to large-scale systems, subject to realistic 10-minute, onshore and offshore

5   wind conditions derived from the numerical mesoscale weather research and forecasting (WRF) model. To reduce computational cost, wind velocity profiles are grouped into k=10 clusters using k-means clustering. Three representative profiles from each cluster are implemented into a nonlinear AWES optimal control model, to determine power-optimal trajectories, system dynamics, as well as instantaneous and cycle-average power. We compare the performance of three different aircraft masses and two sets of nonlinear aerodynamic coefficients for each aircraft size, with wing areas ranging from 10 m^2 to 150 m^2.

10   We predict size and weight-dependent, optimal AWES power curves, annual energy production (AEP) and capacity factor (cf).Tether impacts, such as power losses associated with tether drag and the tether contribution to total system mass are quantified. Furthermore, we estimate a minimum average cycle-average lift to weight ratio, above which ground-generation AWES can operate, to explore the viable AWES mass budget.

1   Introduction

15   Airborne wind energy systems (AWESs) harvest wind energy from the stronger and less turbulent winds at mid-altitude, here defined as heights above 100 m and below 1500 m. These beneficial conditions promise more reliable and stable wind power generation compared to the conventional wind turbines (WTs) at lower altitudes. The light, tower-less design allows for mobile deployment and reduces the capital cost of AWESs (Lunney et al., 2017). These kite inspired systems consist of an autonomous aircraft which is connected to a ground station via tether. While various designs are investigated, two major

20   crosswind concepts are currently considered by industry: the ground-generation also referred to as pumping-mode, and on-board-generation also referred to as drag-mode. This study focuses on the two-phase, ground-generation concept, as it is currently the main concept pursued by industry after Makani Technologies LLC (Makani), the biggest company and proponent of the on-board-generation concept closed in February 2020. On-board-generation AWES carry additional weight with the on-board generator and propeller mass, as well as the heavier, conductive tether. Part of the reason for the closure could have been

25   that the company did not see a viable road to commercialization. Thus a motivation to have a closer look at ground-gen scaling.

One of the biggest companies working on this concept is Ampyx Power (Ampyx). Ground-generation AWES generate power during the reel-out phase while the wing generates large lift forces and pulls the tether from a drum. During the following reel-in phase a fraction of the energy is consumed to return the aircraft back to its initial position and restart the cycle (Luchsinger, 2013). As a result, the power generated by such systems is inherently oscillating which could be offset using multiple devices

30   in a wind farm setup or buffering the energy before feeding it into the grid (Malz et al., 2018).

Over last years two main AWES applications emerged. The first makes use of the mobile nature of the technology which allows the deployment in inaccessible or remote places such as temporary mines or remote off-grid communities as these locations often rely on expensive diesel generators. Second is the grid-scale integration of AWES, which requires upscaling the systems to compete with fossil and renewable energy sources in the energy market. One example is Ampyx Power (Ampyx)

35   which aims to re-power decommissioned offshore wind farms or deploy floating platforms, expecting higher energy yield due to better wind conditions, which in combination with design choices lead to lower levelized cost of electricity. Additionally, setting up AWES offshore allows for safer operation and is likely to be socially more accepted (Ellis and Ferraro, 2016). We therefore investigate the scalability and design space of small to large-scale AWES, both offshore and onshore. Depending on the aircraft's wing surface area, aerodynamic coefficients and the tether diameter, rated power ranges from $\overline{P}_\mathrm{rated} = 145$ kW

40   to 199 kW for $A_\mathrm{wing} = 10$ m^2 and $\overline{P}_\mathrm{rated} = 2010$ kW to 3430 kW for $A_\mathrm{wing} = 150$ m^2. We compare the optimal system performance subject to various wing mass for representative onshore and offshore wind conditions.

In comparison to the commonly used logarithmic wind speed profile, this WRF-derived set of wind data includes the wind direction rotation with height and the complex range of profile shapes emerging from atmospheric stability. This includes almost constant wind velocity profiles associated with unsteady stratification, high sheer wind velocity profiles resulting from stable

45   conditions, as well as non-monotonic wind velocity profiles including low level jets (LLJs). The power output of an AWES not only depends on the wing size, but also the prevalent wind velocity profile shape and magnitude which result in distinct trajectories and operating altitudes. Therefore, a representative wind data set up to mid-altitudes, here defined as heights above 100 m and below 1500 m, is necessary to determine realistic AWES performance. This study relies on mesoscale numerical weather prediction models such as the Weather Research and Forecasting (WRF) model, which is well known for conven-

50   tional WT siting applications (Salvação and Guedes Soares, 2018; Dörenkämper et al., 2020), as measuring wind conditions at mid-altitudes is difficult due to reduced data availability aloft (Sommerfeld et al., 2019a). To reduce the computational cost, 10-minute average wind speed profiles were clustered using the k-means clustering method described in (Sommerfeld, 2020). We compare AWES performance for an onshore location in northern Germany near Pritzwalk (Sommerfeld et al., 2019b) and an offshore location at the FINO3 research platform in the North Sea. These wind clustered wind conditions were implemented

55   into the `awebox` (Leuthold et al., 2020) optimization framework which computes periodic flight trajectories that maximize average mechanical power output.

In comparison to our previous studies, which derived onshore and offshore AWES power curves, this paper explores the AWES design space from small to to utility-scale. We aim at setting up-scaling design and mass targets, instead of a detailed system design. While other studies rely on simplified logarithmic wind speed profiles or reanalysis data sets, we optimize

AWES trajectory subject to realistic 10 minute mesoscale wind data, which allows better optimal performance prediction. This supports decision-making regarding location-specific design, power estimation and scaling limitations.

Section 2 summarizes the onshore and offshore wind resource as well as the clustering results. For a detailed description of the WRF model and clustering algorithm see (Sommerfeld, 2020). Section 3 briefly introduces the AWES model and optimization method as well as the implemented constraints and initialization. Section 4 compares the results for six AWES sizes with three different mass scaling assumptions and two sets of non-linear aerodynamic coefficients. We present, inter alia, trajectories, power curves and annual energy production estimates for for a representative onshore and offshore location. Finally, Section 5 concludes the article with an outlook and motivation for future work to continue to advance AWES towards commercial reality.

2   Wind data

This study considers representative 10 min onshore (northern Germany, lat: $53°10'47.00''$N, lon: $12°11'20.98''$E) and offshore wind data (FINO3 research platform, lat: $55°11,7'$N, lon: $7°9,5'$ E) derived from 12 months of WRF simulations each. Both locations are highlighted by a black dot in figure 1.

Both horizontal velocity components of the resulting mesoscale wind data set are clustered using a k-means clustering algorithm (Pedregosa et al., 2011). According to previous investigations (Sommerfeld, 2020), a small number of clusters with few representative profiles per cluster yield good power and AEP estimates at reasonable computational cost. Therefore, the wind velocity profiles were grouped into k=10 clusters from which the 5th, 50th and 95th percentile (sorted by wind speed at 200 m) were implemented into the optimization algorithm as design points to cover the entire annual wind regime.

The resulting average wind velocity profiles for each of the ten clusters, also known as centroids, are shown in the top row of figure 2. For presentation purposes, only each centroid's wind speed magnitude, colored according to average wind speed up to 500 m, is shown. The complete set of clustered profiles profiles are shown in grey. The cluster average wind profile shapes show wind shears typically associated with unstable and stable conditions. They follow expected location-specific trends with lower wind shear and higher wind speeds offshore (right) in comparison to onshore (left). The associated, color-coded annual centroid frequency is shown in the center. The bottom subfigures summarize the wind speed probability distribution at a reference height of $100 \leq z \leq 400$ m. We chose this reference height as a proxy for wind speed at operating altitude, because an a priori estimation is impossible, and onshore and offshore power curves are almost identical using this reference wind speed. For a detailed description of the WRF model and setup, the clustering process as well as the correlation between clusters and stability conditions see (Sommerfeld, 2020).

3   AWES trajectory optimization model

The investigation of the scaling potential of AWESs not only requires understanding of wind conditions at higher altitudes, but also of AWES power production, which is intrinsically linked to the aircraft's flight dynamics, as the AWES never reaches a
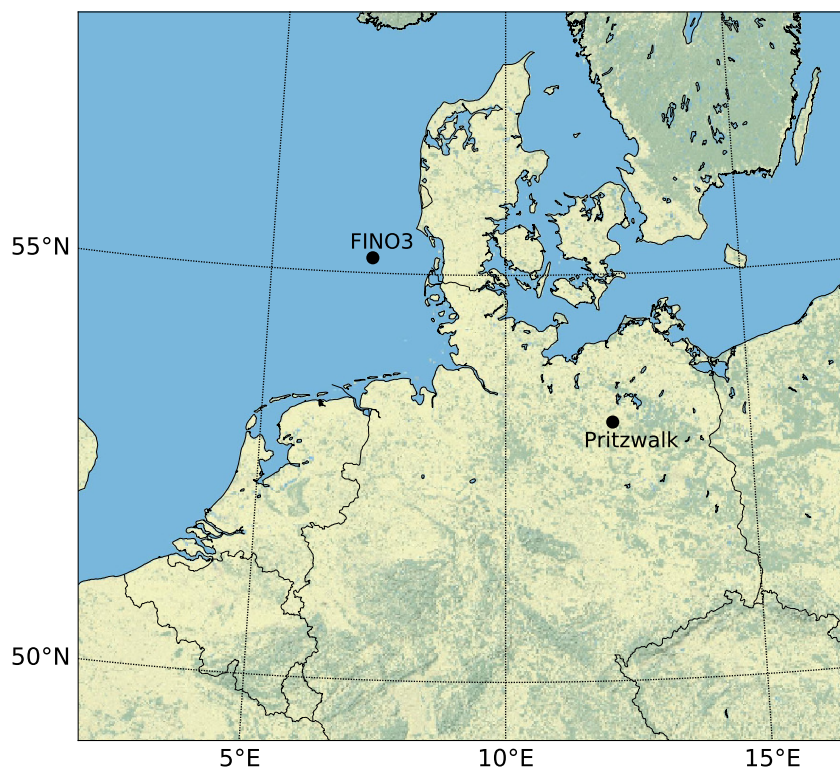
Figure 1. Topography map of northern Germany with the representative onshore (Pritzwalk) and offshore (FINO3) locations highlighted with a black dot.

steady state over the course of a power cycle. Hence power output estimation based on steady-state simplifications are generally not suited for describing the effects of realistic wind profiles or varying system parameters on the power output over the entire operational window. Therefore we make use of optimal control methods to compute power-optimal, dynamically feasible flight trajectories that satisfy operation constraints such as flight envelope and structural system limits.

95 ## 3.1   Model overview

We compute ground-generation AWES power cycles by solving a periodic optimal control problem which maximizes the cycle-average AWES power output $\overline{P}$. In periodic optimal control, the system state at the initial and final time of the trajectory must be equal, but are chosen freely by the optimizer. This methodology, implemented in the open-source software framework `awebox` (Leuthold et al., 2020), is used to generate power-optimal trajectories for single-wing ground-generation AWES sizes
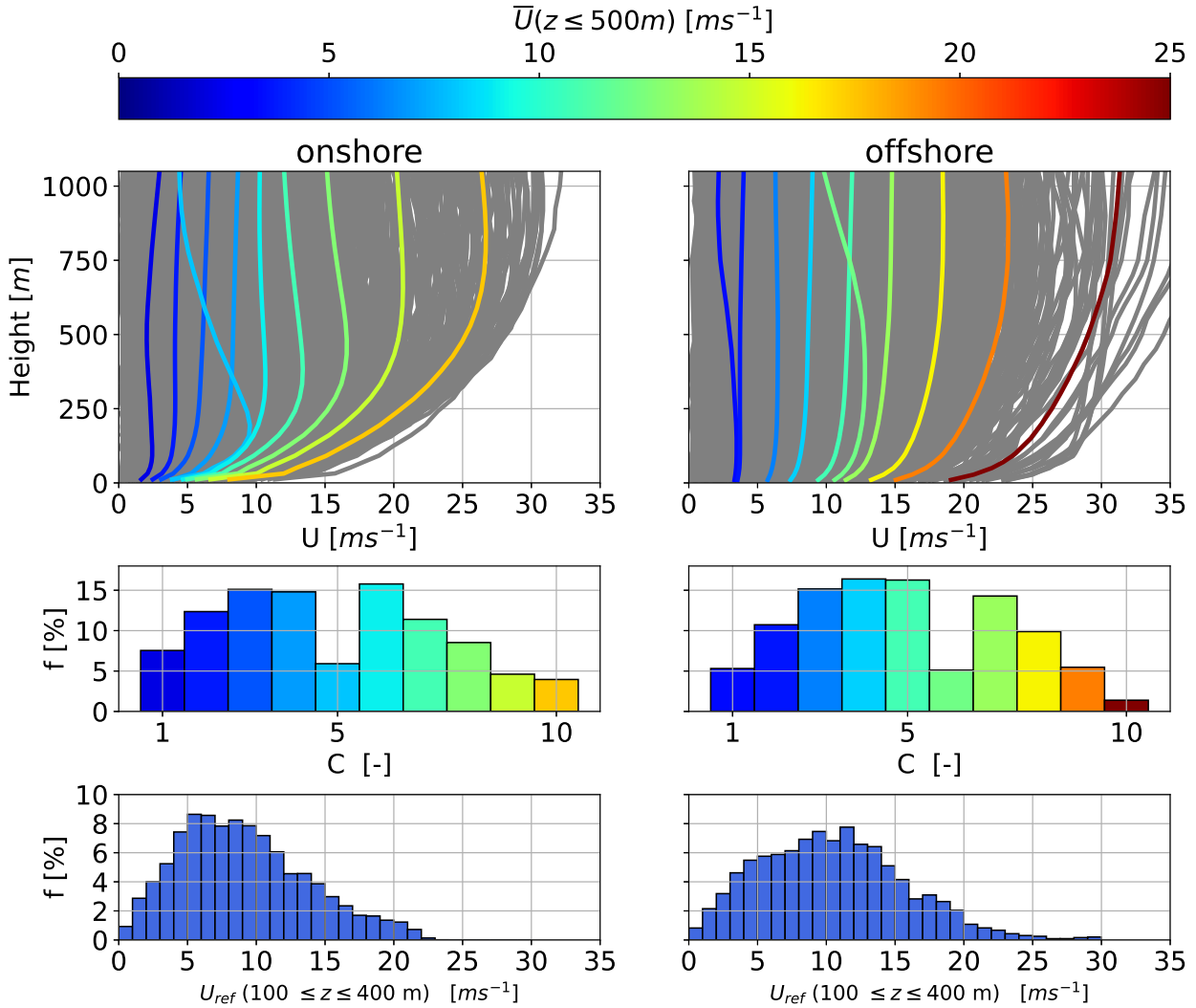
Figure 2. Onshore (left) and offshore (right) annual cluster average wind speed profiles (centroids) resulting from the k-means clustering process for k = 10 (top). Underlying WRF simulated wind speed profiles depicted in grey. The centroids are sorted, labeled and colored in according to average wind speed up to 500 m. The corresponding cluster frequency f for each cluster C is shown in the center. The bottom figures show the wind speed probability distribution between reference heights of $100 \leq z \leq 400$ m.

with various wing area, mass and aerodynamic performance. Table 1 summarizes the imposed constraints for each system design.

The AWES model considers a 6 degree of freedom rigid-wing aircraft model with pre-computed quadratic lift, drag and pitch moment coefficients, which is controlled via aileron, elevator and rudder deflection rates. For this scaling study, the Ampyx

AP2 reference model (Ampyx; Malz et al., 2019) serves as a base from which the aircraft size and mass as well as aerodynamic
105 coefficients were scaled (see sections 3.3 and 3.4).

While the ground station dynamics are not explicitly modeled, constraints on tether speed, acceleration and jerk are imple-
mented to ensure a realistic operating envelope. For this study a reel-out to reel-in ratio of $\frac{2}{3}$ ($\frac{v_{\text{out}}}{v_{\text{in}}} = \frac{10 \text{ ms}^{-1}}{15 \text{ ms}^{-1}}$) was chosen.
Tether acceleration $\dot{l}_{\max} = 10 \text{ ms}^{-2}$ and tether jerk $\ddot{l}_{\max} = 100 \text{ ms}^{-3}$ were limited to simulate generator torque constraints.

For a more detailed description of the model and the optimization algorithm see (Sommerfeld, 2020; Leuthold et al., 2018;
110 De Schutter et al., 2019; Bronnenmeyer, 2018; Horn et al., 2013; Haas et al., 2019).

3.2 Wind profile implementation

The 2D horizontal wind velocity profiles were clustered into k=10 clusters. Three representative profiles from each cluster as
well as each cluster's centroid, rotated such that the main wind direction u points in positive x direction and the deviation
v from it points in positive y direction, were implemented. This assumes omnidirectional AWES operation, which simplifies
115 the comparison of results. We interpolate the u and v components using Lagrange polynomials to obtain a twice continuously
differentiable function representation of the wind velocity profiles, which is necessary formulate an optimal control problem
that can be solved with the gradient-based nonlinear programming (NLP) solver IPOPT (Wächter and Biegler, 2006).

3.3 System scaling

Aircraft mass m and inertia $\mathbf{J}$ are scaled relative to the Ampyx AP2 reference model (Malz et al., 2019; Ampyx) according to
120 simplified geometric scaling laws relative to wing span b (see equation 1). The mass scaling exponent κ ranges from 2.7 to 3.3.
An exponent of 3 represents pure geometric scaling, while $\kappa = 2.7$ implies positive scaling effects and weight savings with
size, while $\kappa = 3.3$ assumes negative scaling. Based on the wing area, maximum tether force and diameter are scaled while
tether speed and acceleration constraints are kept constant.

Makani's openly published technical reports describe their "M600 SN6" as well as their MX2 (*Oktoberkite*) design, which
125 redesigned the M600 air frame to overcome some of its shortcomings and produce $\overline{P}_{\text{MX2}} = 600$ kW at a wind speed of
$U_{\text{MX2}-\text{ref}} = 11 \text{ ms}^{-1}$ at operating height (Echeverri et al., 2020). Note that Makani's on-board-generation concept is inherently
heavier than the ground-generation concept considered here, because of propellers, generators and supporting structures. The
intended M600 design specified a mass of 919 kg, which corresponds to an AP2 mass scaling exponent of $\kappa = 2.72$. The as-
built M600 had a wing area of $A_{\text{wing}} = 32.9 \text{ m}^2$ and a mass $m_{\text{M600}} = 1730.8$ kg. If we scale the AP2 reference aircraft to the
130 same wing area and mass, the corresponding mass scaling exponent is $\kappa = 3.23$. The air frame of the improved MX2 design
aimed at $m_{\text{MX2}} = 1852$ kg for a wing area of $A_{\text{MX2}} = 54 \text{ m}^2$, equivalent to $\kappa = 2.72$ relative to the AP2 reference. Similarly,
WT mass scales with an exponent slightly below 3 based on rotor diameter (Fingersh et al., 2006).

$$m_{\text{scaled}} = m_{\text{ref}} \left(\frac{b}{b_{\text{ref}}} \right)^{\kappa}; \qquad \mathbf{J}_{\text{scaled}} = \mathbf{J}_{\text{ref}} \left(\frac{b}{b_{\text{ref}}} \right)^{\kappa+2} \tag{1}$$

3.4 Aerodynamic scaling

135   Figure 3 shows the aerodynamic performance of the wing model, which includes lift c_L (top left), drag c_D (top center) and pitch moment c_m coefficients (top right) as a function of angle of attack α, lift over drag (bottom left) and glide ratio as a function of angle of attack (bottom center). The bottom right figure shows the $\frac{c_L^3}{c_D^2}$ ratio which determines the theoretical maximum power of any crosswind AWES (Loyd, 1980). Modifications to the AP2 aerodynamic reference model were implemented to assess the impact of improved aerodynamic performance. This is achieved by shifting the c_L, c_D and c_m according to their theoretical

140   behaviour if high lift devices, such as flaps and slats, were attached. Makani's reports mention two shortcomings of their M600 design were the overestimation of c_L^{max} and underestimation of c_D, further justifying this comparison and prompting a more conservative estimation of practical aerodynamic coefficients. Lift and drag at zero angle of attack are increased, stall is delayed, and pitch moment decreased. While both airfoils have comparable optimal glide ratios, the Loyd's optimal power ratio is almost twice as high for the high lift airfoil. Stall effects were implemented for both the AP2 reference model (blue) as

145   well as the high lift (HL - orange) model by formulating a quadratic lift coefficient function (see figure 3). As a result, the lift coefficients deviate slightly in the linear lift region at lower angle of attack.
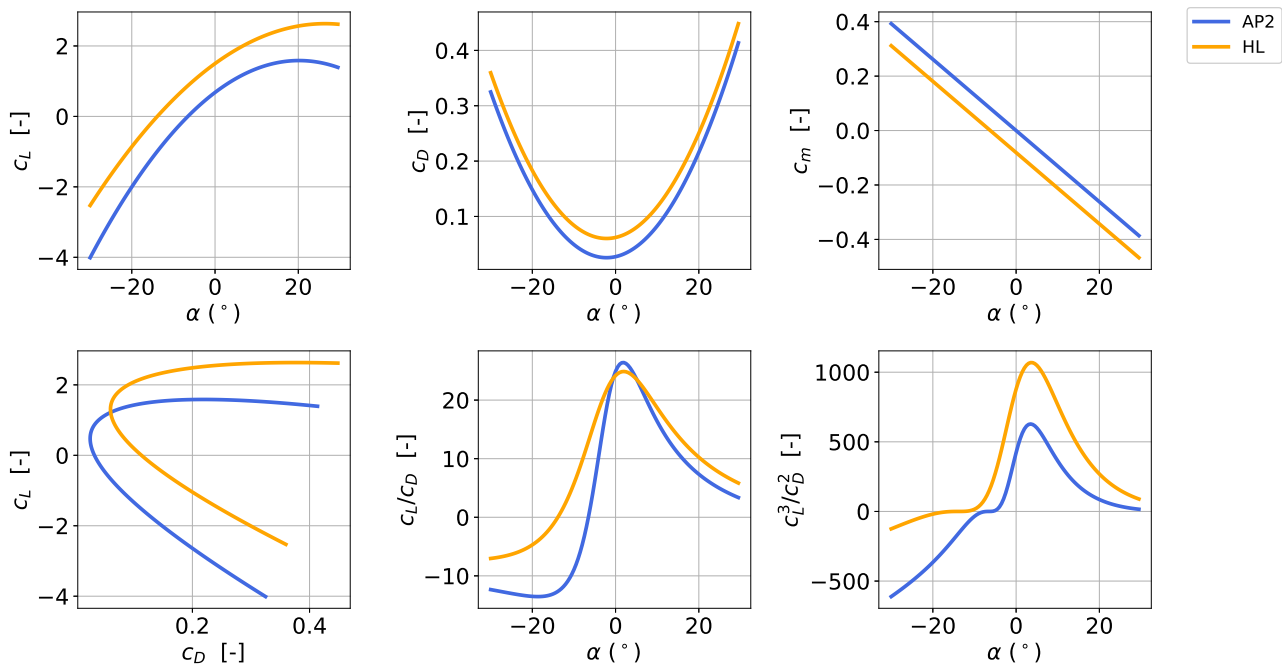
Figure 3. Aerodynamic lift c_L, drag c_D, pitch moment c_m coefficients as a function of angle of attack for reference AP2 (blue) and high-lift (HL) (orange). Aerodynamic efficiency metrics: lift over drag, lift to drag ratio and c_L^3/c_D^2 according to Loyd (Loyd, 1980). HL is derived by modifying the AP2 reference model, in accordance with the theoretical, as if high-lift devices, e.g. flaps and slats were attached.

3.5 Tether model

The tether is modeled as a single solid rod which can not support compressive forces. This is a good assumption when tether tension is high during the power production phase of the power cycle. Total tether drag is proportional to tether diameter
150 d_{tether} and tether length l_{tether}. Both scale with tether tension, assuming a constant tensile strength, and therefore aircraft size and wind speed (see subsection 4.6). The tether drag is approximated by dividing the tether into multiple elements (here $n_{\text{tether}} = 15$) and calculating the apparent wind speed at each element individually, assuming a constant tether drag coefficient of $c_{\text{D}}^{\text{tether}} = 1$. Each elements tether drag is then equally divided between the two endpoints and finally transferred to either the aircraft or ground station. However, this leads to an underestimation of total tether drag at the aircraft (Leuthold et al., 2018).
155 Similarly, the total tether weight W_{tether}, calculated with a constant material density of $\rho_{\text{tether}} = 970 \text{ kgm}^{-3}$, is distributed evenly between the aircraft and ground station.

Tether force constraints are chosen such that the system's rated power is achieved for a logarithmic wind speed profile with $U_{\text{sizing}}(z = 200 \text{ m}) \approx 10 \text{ms}^{-1}$ ($U_{\text{sizing}}(100 \leq z \leq 400 \text{ m}) \approx 10 \text{ ms}^{-1}$), similar to wind at hub height for conventional wind turbines. The tether diameter is calculated assuming a maximum allowable tether stress $\sigma_{\text{tether}} = 3.6 \cdot 10^9$ Pa and a safety
160 factor $SF_{\text{tether}} = 3$.

3.6 Constraints

As previously mentioned, the AWES model solves an optimal control problem to maximize average cycle-power. These constraints include system dynamics, material properties, aircraft and ground station hardware constraints as well as flight envelope limitations. These limitations contain a minimum operating height ($z_{\text{operation}}^{\text{min}}$) as well as a maximum tether length to maintain
165 safe operation. Additionally, an apparent flight speed constraint of $v_{\text{app}} \leq 80 \text{ ms}^{-1}$ for all aircraft sizes was imposed to reduce the mechanical wing load. The maximum tether stress and force, from which the tether diameter is calculated, together with the periodicity constraint are some of the most important path constraints. Ground station hardware limitations such as torque and acceleration dynamics are not explicitly modeled, but implemented as tether speed, acceleration constraints. A fixed angle of attack α and side slip angle β range ensures operation within realistic bounds. However, neither angular constraint is active
170 during flight, because the optimizer tries to achieve an angle of attack close to the maximum of c_{L}, c_{D} and c_{m} (see figure 3). Due to weight and drag effects, actual angle of attack is closer to $\alpha \approx 10°$ during reel-out for the majority of wind speeds.

Table 1 summarizes constraints and system sizes.

3.7 Initialization

The AWES dynamics are highly non-linear and therefore result in a non-convex optimal control problem which possibly has
175 multiple local optima. Therefore, the particular results generated by a numerical optimization solver can only guarantee local optimality, and usually depend on the chosen initialization The optimization is initialized with a circular trajectory based on a fixed number of $n_{\text{loop}} = 5$ loops at a $30°$ elevation angle and an estimated aircraft speed of $v_{\text{init}} = 10 \text{ ms}^{-1}$. Previous analyses showed that the convergence of large AWES highly depends on initial tether length. Larger systems become less sensitive to

Table 1. List of AWES aircraft and tether design parameters for wing areas between 10 and 150 m^2 and flight envelop constraints. AP2 data for reference.

	Parameter	AP2	size 1	size 2	size 3	size 4	size 5	size 6
Aircraft	A_{wing} [m^2]	3	10	20	50	80	100	150
	c_{wing} [m]	0.55	1.00	1.41	2.24	2.83	3.16	3.87
	b_{wing} [m]	5.5	10	14.1	22.4	28.3	31.6	38.7
	AR [-]	10				10		
	$m_{\mathrm{kite}}(\kappa = 2.7)$ [kg]	36.8	185	471	1,624	3,062	4,139	7,155
	$m_{\mathrm{kite}}(\kappa = 3.0)$ [kg]	36.8	221	626	2,473	5,005	6,995	12,850
	$m_{\mathrm{kite}}(\kappa = 3.3)$ [kg]	36.8	265	830	3,767	8,180	11,821	23,079
	α [°]				[-10 : 30]			
	β [°]				[-15 : 15]			
Tether	$l_{\mathrm{tether}}^{\mathrm{max}}$ [m]				2000			
	$\dot{l}_{\mathrm{tether}}$ [ms^{-2}]				[-15 : 10]			
	$\ddot{l}_{\mathrm{tether}}$ [ms^{-2}]				[-15 : 10]			
	$\dddot{l}_{\mathrm{tether}}^{\mathrm{imax}}$ [ms^{-3}]				20			
	$\sigma_{\mathrm{max}}^{\mathrm{tether}}$ [Pa]				3.6 10^9			
	$d_{\mathrm{tether}}(\mathrm{AP2})$ [mm]		5.5	7.8	12.3	15.5	20	21.7
	$d_{\mathrm{tether}}(\mathrm{HL})$ [mm]		7.2	10.2	16.1	20.6	23	28.3
	$F_{\mathrm{tether}}^{\mathrm{max}}(\mathrm{AP2})$ [kN]		34	60	136	241	377	456
	$F_{\mathrm{tether}}^{\mathrm{max}}(\mathrm{HL})$ [kN]		46	94	241	416	499	738
flight envelope	$z_{\mathrm{operating}}^{\mathrm{min}}$ [m]		55	60	75	90	100	125
	$v_{\mathrm{flight}}^{\mathrm{max}}$ [ms^{-1}]				80			

tether drag and hence can drag along a longer tether, because lift to tether drag ratio scales linearly with wing span. Therefore,
180 initial tether length is increased linearly with aircraft wing area (see table 2).

In order to solve the highly nonlinear optimization problem, an appropriate initial guess is generated using a homotopy method similar to those detailed in (Gros et al., 2013; Malz et al., 2020). This technique gradually relaxes the problem from simple tracking of circular loops to the original nonlinear path optimization problem where the previous result serves as an initial guess for the following problem. The resulting problem is formulated in the symbolic modeling framework CasADi for

185 Python (Andersson et al., 2012) and solved using the NLP solver IPOPT (Wächter and Biegler, 2006) in combination with the linear solver MA57 (HSL) .

Table 2. List of AWES optimization initialization values

Parameter		design 1	design 2	design 3	design 4	design 5	design 6
Initialization	N_{loops}				5		
	$\varepsilon\ [^\circ]$				30		
	$l_{\mathrm{tether}}^{\mathrm{init}}\ [\mathrm{m}]$	500	535	643	750	821	1000

4 Results

We compare 6 AWES sizes with three different mass properties and two sets of nonlinear aerodynamic coefficients each to investigate the AWES design space and upscaling potential. Furthermore, we contrast AWES performance at representative

190 onshore (Pritzwalk in northern Germany) and offshore locations (FINO3 research platform in the North Sea) based on one year of WRF simulated and k-means clustered wind data. To that end, we show representative optimized trajectories (subsection 4.1) and compare typical operating altitudes and tether lengths (subsection 4.2). We estimate reaction forces and bending moments based on the assumption of an elliptical lift distribution (subsection 4.3). Subsection 4.4 analyses AWES power curves for each design and determines an AWES power coefficient based on swept area and wing chord. From this we derive the annual

195 energy production (AEP) in subsection 4.5 for each location and system configuration. We examine the predicted power losses (subsection 4.7) due to tether drag. Finally, we establish an upper limit of the weight to lift ratio and compare tether drag forces in subsection 4.6.

4.1 Flight trajectory and time series results

Due to the high level of model and problem non-linearity, the solution of the optimization algorithm can only guarantee local

200 optimality. However, the generated trajectories, shown in figures 4 and A1 (center) for a representative AWES with a wing area of $A_{\mathrm{wing}} = 50\ \mathrm{m}^2$ and $\kappa = 3$ and seem reasonable, are within the set constraints, and are consistent with other studies (De Schutter et al., 2019; Sommerfeld, 2020). It is striking that higher wind speed trajectories above rated power often deviate from the expected trajectory, which occur at lower wind speeds. The system tries to de-power by moving out of the wind window, either upwards or perpendicular to the main wind direction, to stay with in the tether force, tether speed and flight

205 speed constraints, while still maximizing average power. Subsection 4.2 further analyzes the trend towards longer tethers and higher operating altitude with increasing wind speed, which can be seen here as distance from the origin.

The top left sub-figure in figure 4 shows the wind speed profiles U over altitude z (top) with the operating region highlighted in color. Any deviation from the WRF data in grey is caused by the interpolation with Lagrange polynomials during the

implementation process described in subsection 3.2. The hodograph in the bottom left sub-figure shows a top view of the rotated wind velocity components u and v up to a height of 1000 m which follow the expected clockwise rotation with altitude (Stull, 2012).

The four sub-figures on the right display the lift force F_L, tether speed v_{tether}, the apparent, constrained wind speed v_{app} and the instantaneous power p_{current} time series for the corresponding trajectories. Both the production (reel-out) and recovery phase (reel-in) are clearly distinguishable by the transition to negative tether speed and power. Total cycle time seems independent of wind speed and solely determined by the number of loops and tether length used to initialize the optimization. However, previous investigations showed that AWES power output seems to be insensitive to both number of loops (here $n_{\text{loop}} = 5$ for all setups) and flight time.

Looking at the periodic nature of the lift force gives an insight into the load cycles AWES need to withstand during long-term operation. During the production phase the aerodynamic loads oscillate about a constant base load with a periodicity of approximately 8 to 15 seconds depending on aircraft size and wind speed which is comparable to the rotational speed of a conventional wind turbine. Additionally, aerodynamic loads drop to almost zero during the recovery phase as the aircraft returns to it's initial position and the tether is reeled in. Subsection 4.3 further investigates the resulting wing peak loads.

During the production phase tether speed repeatedly drops to zero for an extended period of time, especially at lower wind speeds. This is caused by insufficient lift during the ascent of the aircraft as the system can not produce enough aerodynamic force to pull the tether and overcome gravity. Simultaneously as a consequence power drops to zero and ramps up again, following the flight cycle. To alleviate this inherent intermittency, buffering the energy or coupling multiple, phase-shifted AWES in a wind farm setup would be beneficial (Malz et al., 2018). The reel-out speed only remains positive during the entire production phase at higher wind speeds or for aircraft with higher aerodynamic lift. During the recovery phase tether speed quickly reaches it's minimum of $v_{\text{tether}} = 15 \text{ ms}^{-1}$ to keep this phase as short as possible and reduce power loss. The angle of attack remains moderate to stay close to optimal c_L^3/c_D^2. However, the angle of attack is generally higher than the theoretical optimum to offset the weight and drag of the entire system.

4.2 Tether length and operating altitude

One of the major value propositions of AWESs is that they can tap into wind resources beyond the reach of conventional wind turbines. However, the choice of optimal operating height highly dependents on the wind speed profile and system design. Two opposing effects influence the optimal operating height. On the one hand, an increase in altitude is generally associated with an increase in wind speed and therefore produced power. On the other hand, higher altitudes require a longer tether which result in higher drag losses and also increase the elevation angle which increase gravity-caused "cosine" losses (Diehl, 2013).

Figure 5 shows a trend towards longer average tether lengths $\bar{l}_{\text{tether}}$ (top) and higher average operating altitudes $\bar{z}_{\text{operating}}$ (center) with increasing system size for a representative scaling exponent of $\kappa = 3$ (see equation 1) and wind speed. We chose U_{ref} to be the average wind speed between $100 \text{ m} \leq z \leq 400 \text{ m}$ as we previously found that this range is a good proxy for conditions at operating height (Sommerfeld, 2020). Lighter aircraft and higher lift wings results in slightly higher operating altitudes, a longer tether and higher elevation angle (compare figure A2 in the appendix).
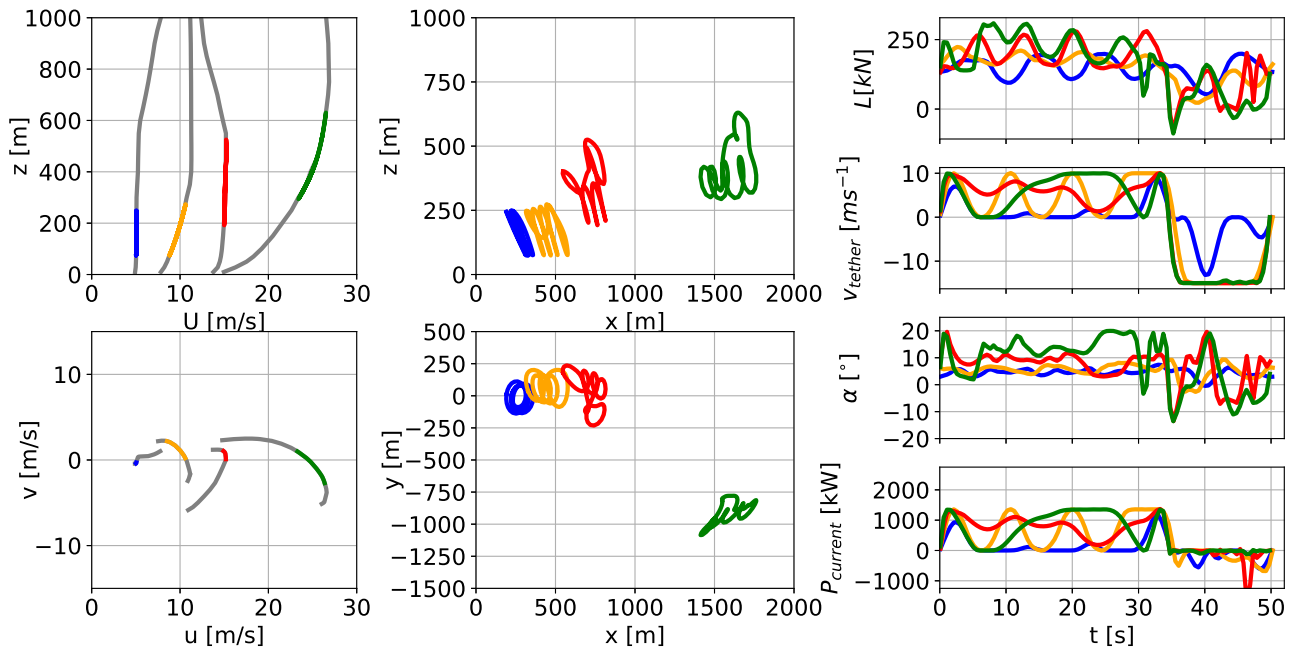
Figure 4. Optimal trajectory and time series for a ground-generation AWES with a wing area of $A_{\mathrm{wing}} = 50\,\mathrm{m}^2$, mass scaling exponent $\kappa = 3$ and AP2 reference aerodynamic coefficients. The left subfigures display representative offshore wind speed profiles (top), and hodograph of wind velocity up to 1000 m (bottom). The deviation of the colored lines is caused by the implementation of discrete WRF-simulated data points using Lagrange polynomials. Trajectories (center) in side and top view. The right subfigures show aerodynamic lift L, tether speed v_{tether}, angle of attack α and instantaneous power P_{current} time series, optimized subject to the corresponding wind velocity profiles.

Outliers, e.g. for high wind speed profiles (compare figure 2), are likely local optima of the highly nonlinear trajectory optimization problem described in section 3.

245   As wind speed increases beyond rated power ($U_{\mathrm{ref}} \approx 10\,\mathrm{ms}^{-1}$, see figures 7 and A3), the aircraft moves out of the wind window to de-power. This is seen as rising average elevation angles $\bar{\bar{\varepsilon}}$ (bottom) above $U_{\mathrm{ref}} = 10\,\mathrm{ms}^{-1}$. Results for both offshore (right) and onshore (left) follow the same trends, but operating heights below rated wind speed are lower offshore because of lower wind shear and higher wind speeds.

It is important to keep in mind that even though the operating height exceeds 500 m for wind speeds of more than $U_{\mathrm{ref}} \approx$
250   $15\,\mathrm{ms}^{-1}$ such wind speeds occur only about 10 % of the time (see figure 2). Between 5 and $15\,\mathrm{ms}^{-1}$, the most likely wind speed range, operating heights both onshore and offshore are between 200 to 300 m. For smaller system sizes these heights are even lower. While this is slightly above the hub-height of current conventional wind turbines, it rebuts the argument of harvesting wind energy beyond this altitude. These findings are consistent with current offshore WT trends, whose rotor diameter increased significantly while hub height only increased marginally over the last years. However, it is likely that offshore hub heights will
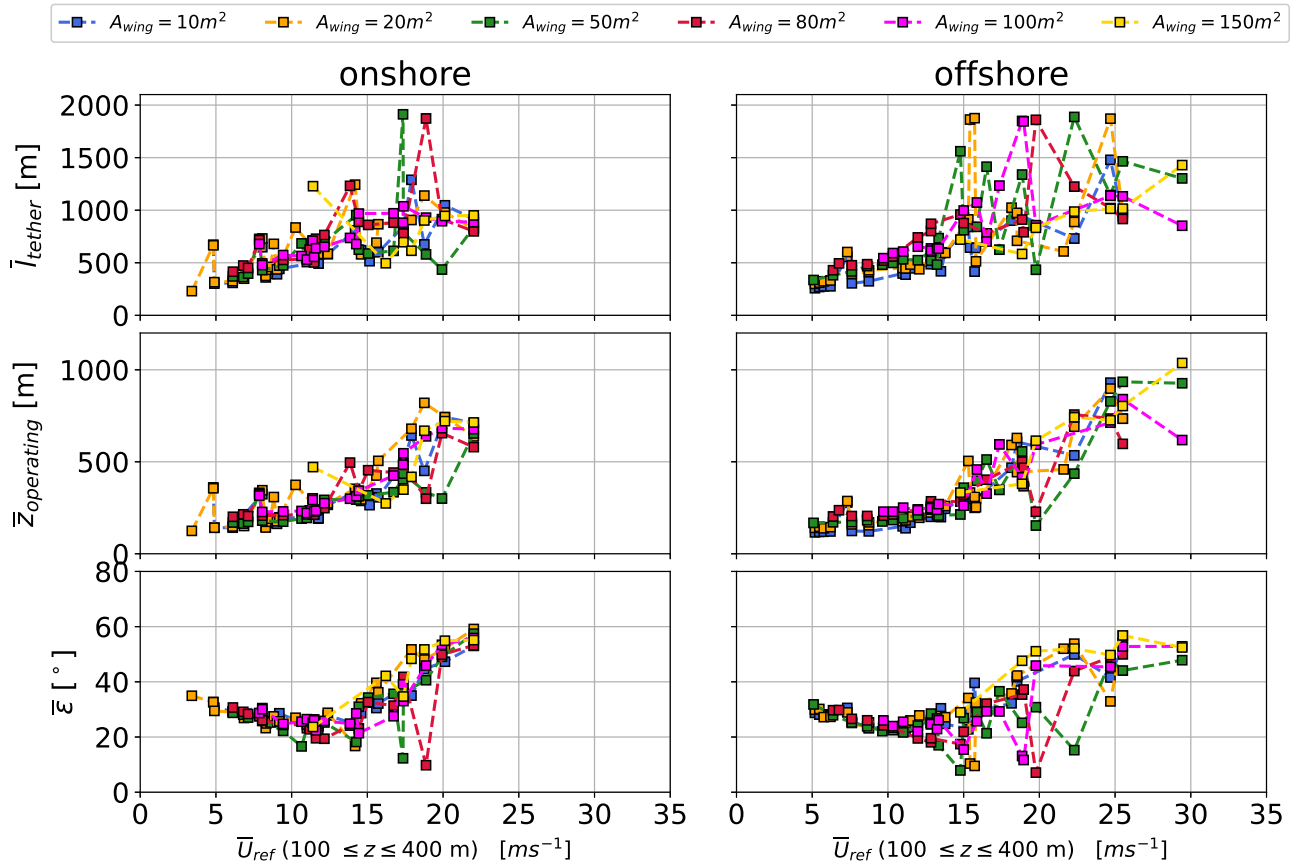
Figure 5. Average tether length $\bar{l}_{\text{tether}}$ (top), average operating altitude $\bar{z}_{\text{operating}}$ (center) and average elevation angle $\bar{\varepsilon}$ (bottom) over reference wind speed $\overline{U}_{\text{ref}}(100 \leq z \leq 400 \text{ m})$. Results for wing areas between $A_{\text{wing}} = 10 - 150 \text{ m}^2$ scaled with a mass scaling exponent of $\kappa = 3$, AP2 reference aerodynamic coefficients for both onshore (left) and offshore (right) location.

255   increase as technology improves, making the argument for the deployment of AWES particularity challenging as both operate at comparable heights and WT are the more proven and established technology. However, this might be different for multiple kite systems which could benefit from longer tethers, due to reduced tether motion (De Schutter et al., 2019).

4.3 Reaction forces and moments

We analyze wing loads since detailed design of the aircraft and wing box is beyond the scope of this paper. Weight is neglected
260   as it is an order of magnitude smaller than the aerodynamic lift force. We assume an elliptic lift distribution (equation: 2 (Torenbeek and Wittenberg, 2009)) which results in a normalized line load of $\tilde{l}$, normalized shear force $\tilde{V}_{\text{Lift}}$ and normalized

bending moment $\tilde{M}_{\mathrm{Lift}}$. Loads are normalized by their maximum value at the wing root (l_0, V_0, M_0) to obtain generalized trends independent of wing size.

$$l = l_0 \sqrt{1 - (\tilde{y})^2} \tag{2}$$

265   Figure 6 visualizes the maximum cycle-average loads at the wing root, which can be used to scale the normalized load distributions along the wing, for both sets of aerodynamic coefficients, all three mass scaling exponents κ and aircraft wing area A_{wing}. Aerodynamic line loads l_0 (top) scale favorably with wing area as they only scale with wing span, while total shear force V_0, equivalent to total lift force, scales linearly with wing area. In contrast, bending moment M_0 scales with area and wing length.

270   Higher aerodynamic lift coefficients (HL: circle) result in higher aerodynamic loads in comparison to the AP2 reference model (AP2: square). Heavier aircraft with higher mass scaling exponent κ (subsection 3.3) also result in higher aerodynamic loads as they require more lift to ascent which results higher average aerodynamic forces. Data for an aircraft with an area of $A_{\mathrm{wing}} = 150 \, \mathrm{m}^2$ and $\kappa = 3.3$ are missing as the optimization could not find a feasible solution.
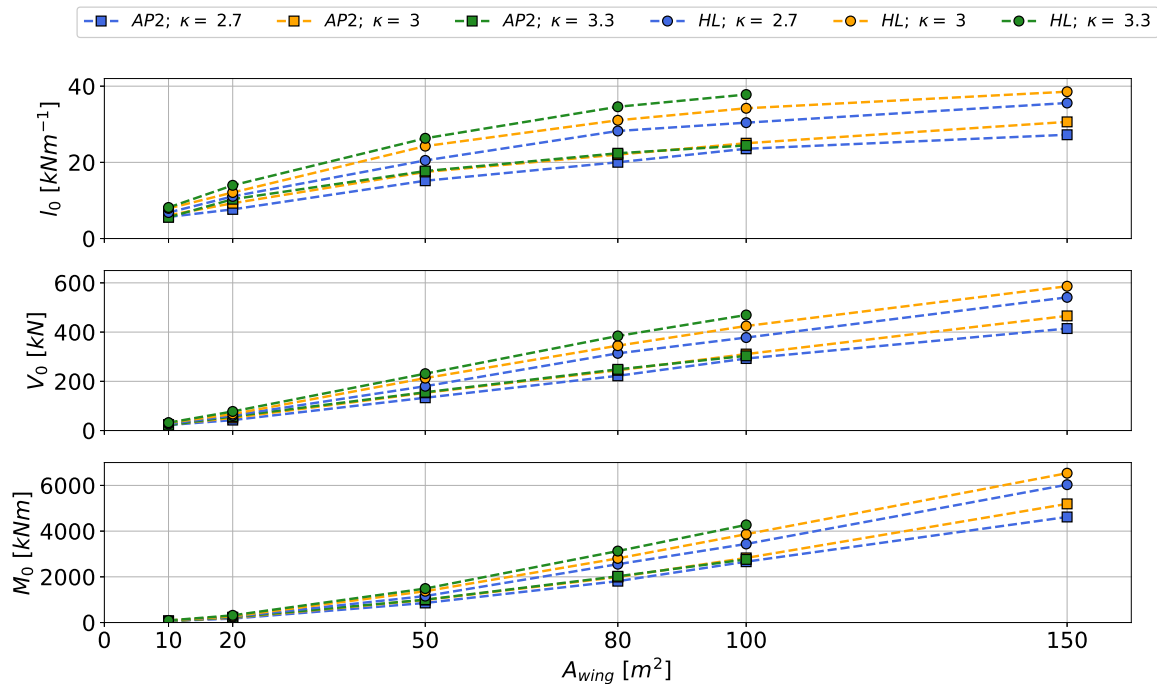
Figure 6. Maximum cycle-averaged aerodynamic wing line load l_0 (top), shear force V_0 (center) and bending moment M_0 (bottom) at the wing root over wing area A_{wing}. Summarizes data for both sets of aerodynamic coefficients (HL: circle, AP2: square) and all three mass scaling exponents $\kappa = 2.7, 3, 3.3$.

4.4 Power curve

275 This section investigates a representative cycle-average AWES power curve for all sizes and estimates an AWES power coefficient $c_\mathrm{p}^\mathrm{AWES}$ as a function of swept area. For visualization purposes, only data for the offshore location, a mass scaling exponent of $\kappa = 2.7$ and HL aerodynamic coefficients are shown here. Other results follow similar trends. Some can be found in the appendix in figure 7 and A3.

Plotting the cycle-average power $\overline{P}$, derived from 3 representative profiles from each of the 10 wind velocity clusters, over 280 reference wind speed produces typical wind power curves as seen in figure 7 (top). As of now, no standard reference wind speed U_ref, equivalent to wind speed at hub height for conventional WT, has been agreed upon for AWES. Furthermore, using this altitude range results in comparable power curve trends onshore and offshore.

Table 3 summarizes the rated power $\overline{P}_\mathrm{rated}$ for AWES between 10 and 150 m^2 scaled with a mass scaling exponent of $\kappa = 2.7$. The table also displays the equivalent WT rotor diameter $D_\mathrm{WT}^\mathrm{equiv}$, for an assumed power coefficient of $c_\mathrm{p}^{WT} = 0.4$ and 285 a rated wind speed of 10 ms^{-1}, as reference. The system size and therefore material cost benefits of AWES become obvious when comparing AWES wing span b_wing to WT rotor diameter $D_\mathrm{WT}^\mathrm{equiv}$. AWES wing span is about 30 (HL) to 40 % (AP2) of the equivalent rotor diameter.

Table 3. Rated AWES power for wing areas between 10 and 150 m^2 scaled with a mass scaling exponent of $\kappa = 2.7$. Equivalent wind turbine rotor diameter for an assumed power coefficient of $c_\mathrm{p}^{WT} = 0.4$ and a rated wind speed of 10 ms^{-1}.

$A_\mathrm{wing}[\mathrm{m}^2]$	10		20		50		80		100		150	
$b_\mathrm{wing}[\mathrm{m}]$	10		14.1		22.4		28.3		31.6		38.7	
aerodynamic coeff.	AP2	HL	AP2	HL	AP2	HL	AP2	HL	AP2	HL	AP2	HL
$\overline{P}_\mathrm{rated}$ [kW]	145	200	265	420	575	1030	1045	1800	1600	2225	2000	3400
$D_\mathrm{WT}^\mathrm{equiv}$ [m]	27	32	37	47	55	73	74	97	91	108	102	132

Missing data in figure 7 originate from an infeasible combination of constraints and boundary conditions, mostly related to a heavy aircraft and insufficient wind speeds. This results in a minimal cut-in wind speed for each system. However, instead of a 290 gradual increasing from zero, the optimizer finds a feasible solution above cut-in wind speed with power closer to rated power (see $A_\mathrm{wing} = 80, 100$ m^2 in figure A4 or $A_\mathrm{wing} = 150$ m^2 in figure 7). Higher system mass does not seem to affect rated power, which is determined by tether tension and tether speed constraints (i.e. no direct generator constraint) only cut-in wind speed. No cut-out wind speed limitations were implemented. Therefore, wind power is only limited by each location's maximum wind speed, which is significantly higher offshore (compare figure 2). All system sizes reach rated power at about $U_\mathrm{ref} = 10$ ms^{-1}, 295 because the tether diameter of each AWES configuration was sized for this reference wind speed (see subsection 3.5). We defined the same tether diameter for both onshore and offshore location. However, offshore AWES design could benefit from a larger tether diameter as wind speeds are generally higher (see figure 2). This would result in higher rated power and a higher AEP (see subsection 4.5). Higher lift coefficients result in higher rated power and a steeper power increase up to rated power.

Power variations are caused by local optima mostly occurring above rated wind speed as the system de-powers to stay within
300   tether force and flight speed constraints (see subsection 3.6).

In contrast to (Sommerfeld, 2020) the flight path length l_{path} (figure 7 second from top) remains almost constant with
wind speed. In comparison to this previous study overall path length is lower, which is probably due to the lower mass scaling
exponent of $\kappa = 2.3$. Path length increases with system size and mass due to higher inertia, longer tether length and an increased
minimal turning radius.
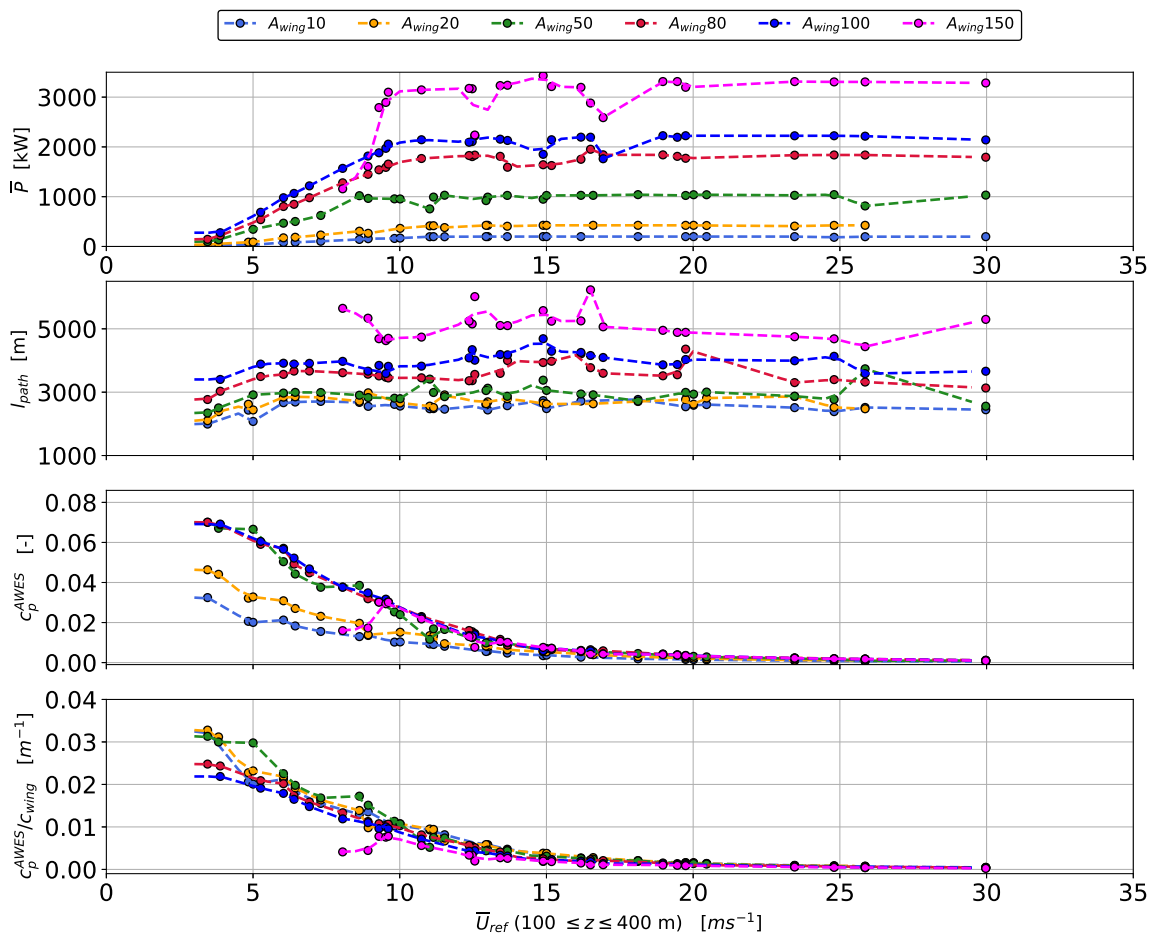
Figure 7. Power curve (top), path length (second from top), AWES power coefficient $c_{\mathrm{p}}^{\mathrm{AWES}}$ (third from top) and AWES power coefficient
divided by chord length $c_{\mathrm{p}}^{\mathrm{AWES}}/c_{\mathrm{wing}}$ (bottom) over reference wind speed $100 \leq z \leq 400$ m for AWESs with $A_{\mathrm{wing}} = 10 - 150$ m^2 and
HL aerodynamic coefficients. Data is derived from p5, p50, p95 wind velocity profiles within each of the k=10 offshore clusters. Missing
data points are the result of infeasible combination of optimization constraints and boundary conditions.

305   We estimate AWES power coefficients $c_{\mathrm{p}}^{\mathrm{AWES}}$ to simplify the AWES power estimation and to compare AWES performance.
We derive the power coefficient (see equation 3) from the cycle average power $\overline{P}$, the swept area A_{swept} (wing span b_{wing}
multiplied by path length l_{path}) and reference wind speed U_{ref}, similar to conventional WTs. Since determining the wind speed
along the flight path before deployment is impossible, we use average wind speeds between $100\,\mathrm{m}$ and $400\,\mathrm{m}$ as a proxy. The
resulting trends shown in figure 7 (third from top) decrease non-linearly with wind speed, which can be attributed to different

310 trajectories and increased losses associated with a longer tether, i.e. tether drag and weight. The AWES power coefficients
seem to converge for wing areas larger than $A_{\mathrm{wing}} \geq 50\,\mathrm{m}^2$, while $c_{\mathrm{p}}^{\mathrm{AWES}}$ of the smallest two aircraft sizes $A_{\mathrm{wing}} = 10, 20\,\mathrm{m}$
are significantly lower. A possible explanation is that smaller wings have a higher tether drag to lift force ratio, which might
reduce the power coefficient. As expected, aerodynamic efficiency highly affects AWES power coefficients, with HL values
almost doubling in comparison to the AP2 reference (compare figure 7 with A3 in the appendix).

315   Scaling the power coefficients with each system's wing chord c_{wing} collapses results onto a single curve (bottom). A possible
explanation for this is that the mechanical power of a ground-generation AWES, which is the product of tether force and tether
speed, scales with both wing area and path length. Path length increases with system size, but total cycle times remain almost
constant, which results in an increased average flight speed (see subsection 4.1).

$$c_{\mathrm{p}}^{\mathrm{AWES}} = \frac{\overline{P}}{\frac{\rho_{air}}{2} A_{\mathrm{swept}} U_{\mathrm{ref}}^3} = \frac{\overline{P}}{\frac{\rho_{air}}{2} b_{\mathrm{wing}} l_{\mathrm{path}} U_{\mathrm{ref}}^3} \qquad (3)$$

320 ## 4.5   AEP

We estimate the annual energy production (AEP) and capacity factor cf (equation 4) from the previously described power curve
$\overline{P}$ (subsection 4.4) and annual wind speed probability distribution f, derived from the histogram of annual wind speeds seen
in the bottom subfigure of figure 2.

     Rated power P_{rated} is defined from optimization results, as the a priori estimation of nonlinear, trajectory dependent losses
325 is difficult.

$$\mathrm{AEP} = \sum_{i=1}^{k} \left(\overline{P}_i f_i \right) \, 8760 \, \frac{\mathrm{h}}{\mathrm{year}} \qquad\qquad \mathrm{cf} = \frac{\overline{P}_i f_i}{P_{\mathrm{rated}}} \qquad (4)$$

     Figure 8 compares the impact of aerodynamic efficiency by contrasting the previously described power curve (top) for
AWESs with a wing area of $A_{\mathrm{wing}} = 50\,\mathrm{m}^2$ and a mass scaling exponent of $\kappa = 2.7$. Data for high lift aerodynamic coefficients
are highlighted by a circle while AP2 reference data is marked by a square. Wind conditions are the p5, p50, p95 percentile
330 onshore (blue) and offshore (orange) wind velocity profiles for each of the k=10 clusters. The center sub-figure summarizes the
wind speed probability distribution between $100 \leq z \leq 400\,\mathrm{m}$ which stands in as a proxy for wind at operating altitude (see
section 2). As expected, higher wind speeds are more likely to occur offshore (FINO3) than onshore (Pritzwalk). However,
very high wind speeds above $U_{\mathrm{ref}} > 18 - 20\,\mathrm{ms}^{-1}$, beyond the cut-off speed of realistic wind energy converters, have a very
low chance occurrence at both locations. The resulting annual average energy production distribution $\overline{E}$ (bottom) reveal a clear

335 difference between the offshore and onshore energy potential. Better wind conditions offshore lead result in higher AEP and cf. Higher aerodynamic efficiency increases rated power and power up to rated wind speed. Therefore, AEP and cf almost doubles for HL in comparison to the AP2 reference, highlighting the importance of exploring high lift configurations.
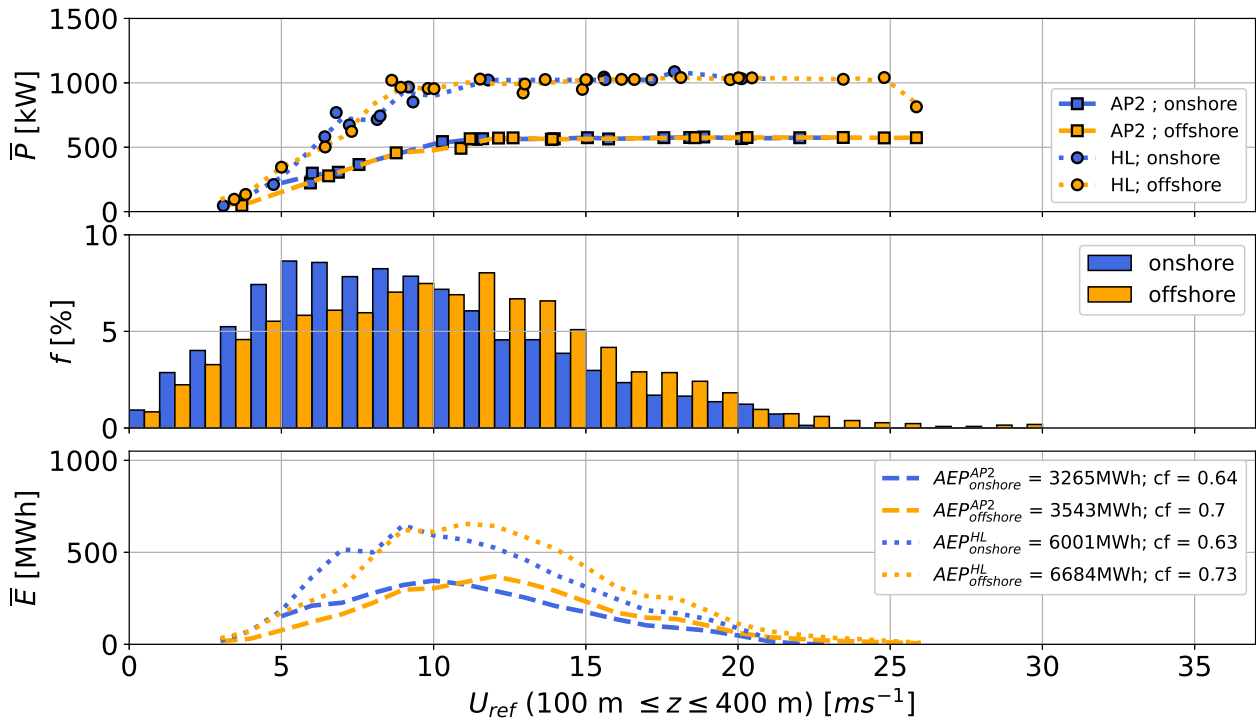
Figure 8. Representative AWES power curves (top) for both sets of HL (circle) and AP2 (square) reference aerodynamic coefficients for both onshore (blue) and offshore (orange) location. The masses of the $A_{\text{wing}} = 50 \text{ m}^2$ wing area aircraft are scaled according to equation 1 with a mass exponent of $\kappa = 2.7$. Cycle-average power $\overline{P}$ is derived from p5, p50, p95 wind velocity profiles within each of the k=10 WRF-simulated clusters. A reference height of $100 \le z_{\text{ref}} \le 400 \text{ m}$ is used as a proxy for wind speed at operating altitude to calculate the annual wind speed probability distribution (center). The integral over the annual energy production distribution (bottom) which is the product of power and wind speed probability distribution, yields the AEP (legend).

Figure 9 compares the AEP and cf estimates for all system sizes scaled with a mass scaling exponent of $\kappa = 2.7$. AEP increases almost linearly with wing area (top), because power, which is the product of tether force and tether speed, scales with 340 wing area. Tether force scales linearly with wing area and maximum tether speed is kept constant throughout all optimization runs. As expected HL aerodynamic coefficients (circle) outperform the AP2 reference (square). Offshore (orange) AEP and cf is generally higher than onshore (blue) because higher wind speeds are more likely. Overall cf (bottom) remains almost unchanged for wing sizes up to $A_{\text{wing}} = 100 \text{ m}$ and sharply declines for $A_{\text{wing}} = 150 \text{ m}$, due to the high number of infeasible solutions at lower wind speeds, equivalent to not being able to fly due to weight (see figure 7). The relatively high cf values

345 are caused by the relativity low rated wind speed of $U_{\text{rated}} = 10 \text{ ms}^{-1}$. This leads to a design trade-off between generator size relative to wing area and tether diameter, similar to conventional WT.

Onshore AEP and cf seems to outperform offshore for wing areas larger than 100 m^2. This is likely caused by outliers, or wind velocity profile specific local minima, in the power curve (compare to power curve figure A5 in appendix) before rated wind speed ($v_{\text{rated}} = 10 \text{ ms}^{-1}$), where the system seemingly overperforms.
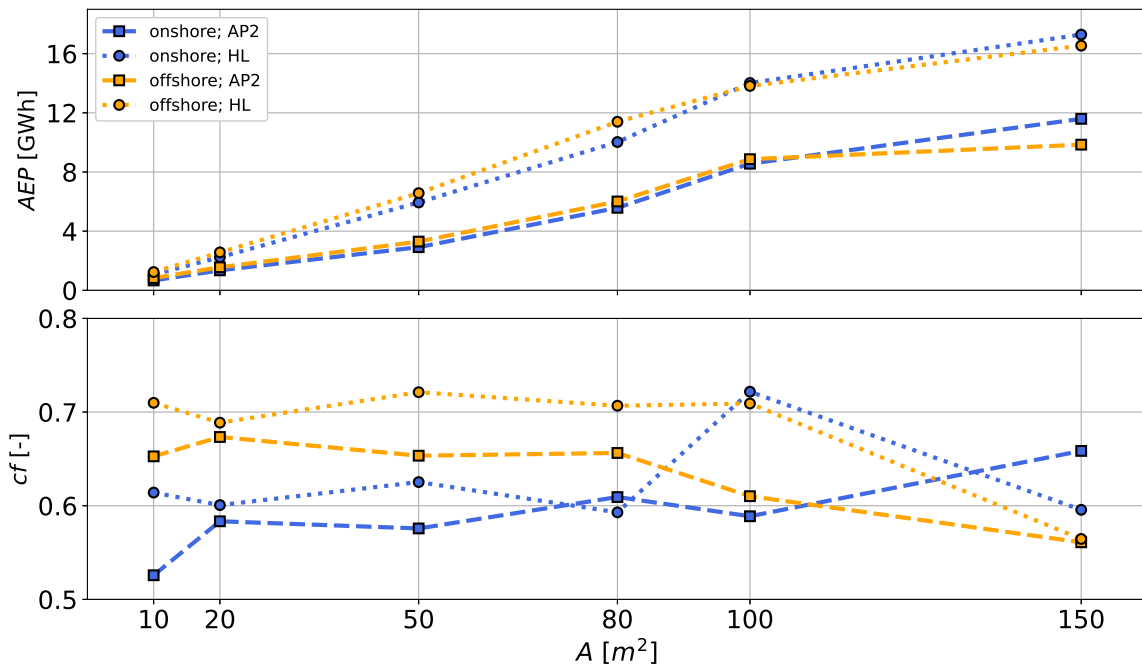
Figure 9. Representative AWES AEP (top) and cf (bottom) over aircraft wing area A_{wing} scaled according to equation 1 with a mass exponent of $\kappa = 2.7$. Figure summarizes data for both sets of HL (circle) and AP2 (square) reference aerodynamic coefficients as well as both onshore (blue) and offshore (orange) location. Results are based on the cycle-average power $\overline{P}$ derived from p5, p50, p95 wind velocity profiles within each of the k=10 WRF-simulated clusters and wind speed probability distribution between $100 \leq z_{\text{ref}} \leq 400$ m, used as a proxy for wind speed at operating height.

350 Figure 10 compares AEP for a mass scaling exponents of $\kappa = 2.7$ to scaling with $\kappa = 3$ and $\kappa = 3.3$, both onshore and offshore. Heavy configurations with no feasible trajectory at any wind speed result in missing data. While smaller systems seem almost unaffected by aircraft weight, mass scaling effects lead to significant reduction in AEP for larger AWES. This is particularly true for wings with aerodynamic reference coefficients (AP2, square) and onshore wind conditions. Combining results from both figure 9, which already shows diminishing returns in AEP and cf with increasing wing area for the lightest,

355 idealized aircraft mass scaling, and figure 10, which predicts that AEP will only decline for heavier mass scaling, conveys that upscaling AWES is only beneficial with significant weight reduction. These results hint at the existence of an upper limit of

AWES weight relative to AWES size or lift (see subsection 4.6), which is plausible since mass scales with aircraft volume and lift scales with aircraft area. Therefore and for compensating power fluctuation caused by the cyclic nature of ground-generation AWES, it is likely better to deploy multiple smaller scale devices rather than a single large-scale system. Determining the ideal,
360   site-specific AWES size needs to be determined by realistic mass scaling and the local wind resource.
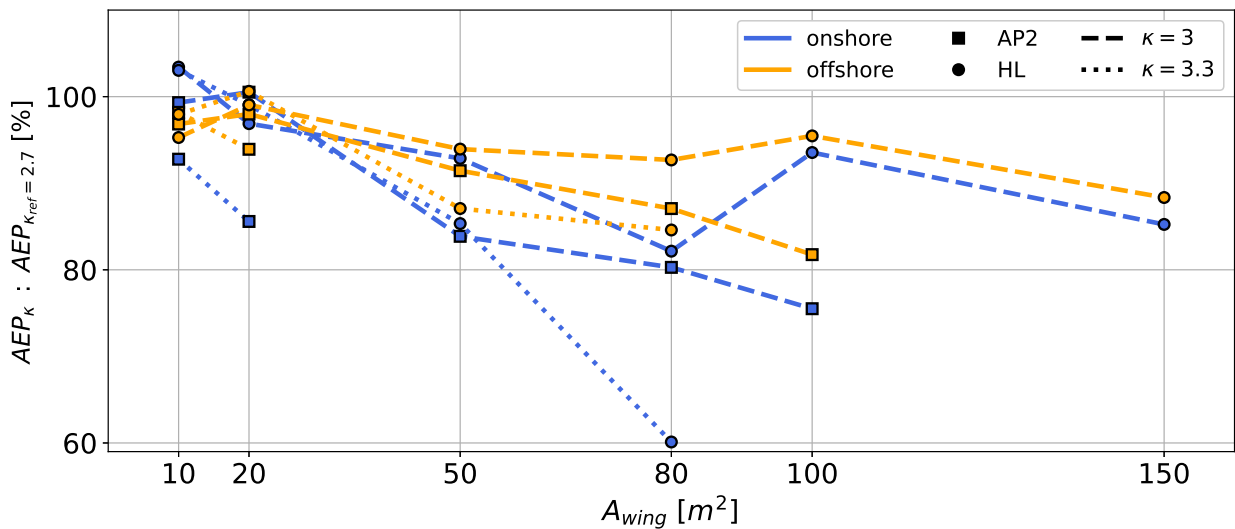
Figure 10. AEP ratio for mass scaling exponent $\kappa = 3$ (dashed lines) and $\kappa = 3.3$ (dotted lines) relative to AEP of $\kappa = 2.7$ over aircraft wing area A_{wing}. Figure summarizes data for both onshore (blue) and offshore (orange) location as well as both sets aerodynamic coefficients HL (circle) and AP2 (square). Results are based on the cycle-average power $\overline{P}$ derived from p5, p50, p95 wind velocity profiles within each of the k=10 WRF-simulated clusters. Missing data points indicate that no feasible solution for any wind velocity profile was found.

4.6   Weight and drag impact

The most effective AWES concept benefit from increased apparent wind speed during crosswind flight (Loyd, 1980), such as the ground-generation concept investigated in this study. Such crosswind trajectories, whether circular or figure-of-eight, always include an ascent during each loop where the aircraft needs to overcome gravity to gain altitude. This leads to a deceleration
365   and therefore reduction of aerodynamic lift. AWESs with excess mass fail to overcome weight and drag and can no longer climb.

   With an increased wing area, the entire aircraft, particularly the load carrying structures such as the wing box, need to increase in size and weight in order to withstand increased aerodynamic loads produced. Aircraft mass scales with volume ($m_{\mathrm{aircraft}} \sim b^3$; wing span b), assuming pure geometric scaling without design improvements, while lift force and therefore
370   power only scales with the wing area ($F_{\mathrm{lift}} \sim b^2$). Similarly, conventional WT power and AEP scales with the rotor diameter square, while theoretic WT mass scales with the cube of the rotor diameter (Gasch and Twele, 2012). However, comparing both wind energy converters under these assumptions, AWES perform worse as their flight path degrades with increasing system

size and mass. This can be attributed to the fact that AWES need to produce enough lift to carry their own weight to operate, while WT are supported by a tower.

375   These facts limit AWES size. The prevailing wind resource does not improve enough within the lower parts of the atmosphere to produce sufficient aerodynamic lift to overcome the increased system drag and weight, associated with larger systems. Wind speed only increases marginally with height, especially offshore or at times of unstable of neutral stratification (compare figure 2). Furthermore, higher operating altitudes also lead to increased "cosine losses", unless offset by a longer tether which in turn results in more drag and weight. Better aerodynamics or lighter, more durable aircraft and tether materials can only push this

380   boundary, but not overcome it.

    A comparison of tether weight W_{tether} during the production phase (reel-out) to total system weight ($W_{\text{total}} = W_{\text{aircraft}} + W_{\text{tether}}$) in figure 11 (top) shows that the tether makes up 10 to 30 % of the entire system weight during these times. Note that the tether cross sectional area is sized with a safety factor of 3. Tether cross sectional area mostly scales with aerodynamic force and therefore wing area, while the aircraft weight scales with a mass scaling exponent $\kappa = 2.7, \ 3.0, \ 3.3$ which results in

385   decreasing trend lines. This value is higher for high lift airfoils (circle) as the tether diameter is larger to withstand the higher aerodynamic forces. For lighter aircraft, scaled with $\kappa = 2.7$ (dash-dotted), the portion of tether weight is higher, because the tether diameter remains constant while the aircraft mass is lighter.

    The bottom sub-figure reveals that tether drag makes up about 15 to 40 % of the entire system drag during the production phase. Tether diameter d_{tether} and therefore face area ($A_{\text{tether}}^{\text{face}} = d_{\text{tether}} l_{\text{tether}}$) scales beneficially with wing area, leading to

390   the downward trend. For this evaluation half the simulated tether drag is attributed to the aircraft and the other half to the ground station. More detailed models could explore the impact of tether dynamics and tether drag in more detail.

    It is critical for crosswind AWES to ascend during each loop of the production or reel-out phase. The aircraft needs to produce enough aerodynamic lift, which decreases as the aircraft slows down during ascent (compare 4), to overcome gravity and maintain tether tension. The top sub-figure in figure 12 contrasts the AWES equivalent of the aeronautic load factor,

395   here defined as the ratio of average lift force $\overline{L}_{\text{wing}}$ to total AWES weight $\overline{W}_{\text{total}}$, including aircraft and tether mass (cross sectional safety factor of 3), during the reel-out phase for all aircraft sizes $A_{\text{wing}} = 10 - 150 \ \text{m}^2$, mass scaling exponents $\kappa = 2.7, \ 3.0, \ 3.3$ and aerodynamic coefficients HL, AP2. The average load factor decreases from about 10 - 20 to 10 - 5, depending on aerodynamic performance and mass scaling, which is approximately the maneuvering load factor of an acrobatic airplane $n_{\text{acrobatic}} = 6.0$ (Federal Aviation Agency, 2017). For utility airplanes this value is about $n_{\text{utility}} = 4.4$. The beneficial

400   effect of better aerodynamics and mass scaling are clearly visible in a higher lift to weight ratio. High system mass with insufficient lift on the other hand leads to infeasible solutions and missing data.

    The bottom sub-figure of figure 12 shows a slight increase of average lift $\overline{L}_{\text{wing}}$ to total average drag $\overline{D}_{\text{total}}$ (including tether drag) ratio with increasing wing area. Overall however, this ratio remains almost constant around 14 - 15. The decrease for $A_{wing} = 100, 150 \ \text{m}^2$, $\kappa = 3$ and AP2 aerodynamics is likely caused by local optimization minima and few feasible wind

405   speed profiles. For this investigation half the tether drag is assigned to aircraft and the other half to ground station.

    No feasible solution of too heavy aircraft lead to missing data points. For example, no feasible solution could be found for a large-scale aircraft with an area of $A_{\text{wing}} = 150 \ \text{m}^2$, scaled with the lightest mass scaling exponent of $\kappa = 2.7$, and AP2
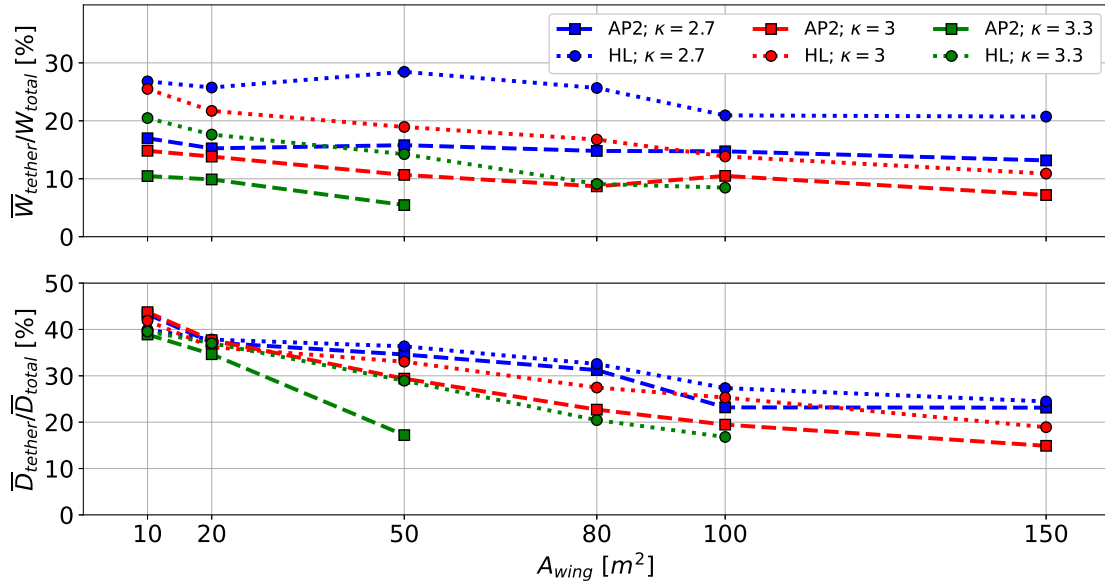
Figure 11. Percentage of cycle-average tether weight $\overline{W}_{\text{tether}}$ to total weight $\overline{W}_{\text{total}}$ (top) and tether drag $\overline{D}_{\text{tether}}$ to total drag $\overline{D}_{\text{total}}$ (bottom) during production phase (reel-out) for all aircraft sizes $A_{\text{wing}} = 10 - 150 \, \text{m}^2$, sets of aerodynamic coefficients AP2, HL and mass scaling exponents $\kappa = 2.7, \, 3, \, 3.3$ for wind data at the offshore location.

reference aerodynamic coefficients at low wind speeds $U_{\text{ref}} < 5 \, \text{ms}^{-1}$. This can be seen in figure 13 which shows the average lift $\overline{L}_{\text{wing}}$ to total weight $\overline{W}_{\text{total}}$, including tether and aircraft, ratio for all aircraft sizes with AP2 reference aerodynamic scaled

410   with $\kappa = 2.7$ over reference wind speed . Lift to weight ratio increases up to $U_{\text{ref}} \approx 5 \, \text{ms}^{-1}$, above which it remains almost constant. This can likely be attributed to the applied apparent flight speed constraint of $U_{\text{app}}^{\max} = 80 \, \text{ms}^{-1}$ which seems to already be achieved at this reference wind speed. These data suggest that the minimum viable load factor is about 5 (equivalent to a maximum viable weight to lift ratio of 20 %) for the given flight speed constraint.

The bottom subfigure of figure 13 shows the lift $\overline{L}_{\text{wing}}$ to total drag $\overline{D}_{\text{total}}$, including tether drag, ratio over reference wind

415   speed for all aircraft sizes scaled with $\kappa = 2.7$ and AP2 reference aerodynamic coefficients. Data for all aircraft sizes show a similar trend with the lift to drag ratio halving from about 20 to 10. This decrease is primarily caused by longer tether lengths at higher wind speeds (compare figure 5), which results in more drag and weight. Heavier system weight also leads to an angle of attack α increase as the aircraft needs to produce more lift.

4.7 Power losses

420   Increased aircraft wing area not only leads to increased power potential, but is also accompanied by increased tether losses due to weight and drag. Tether mass scales with aircraft wing area, because higher aerodynamic force requires a larger tether
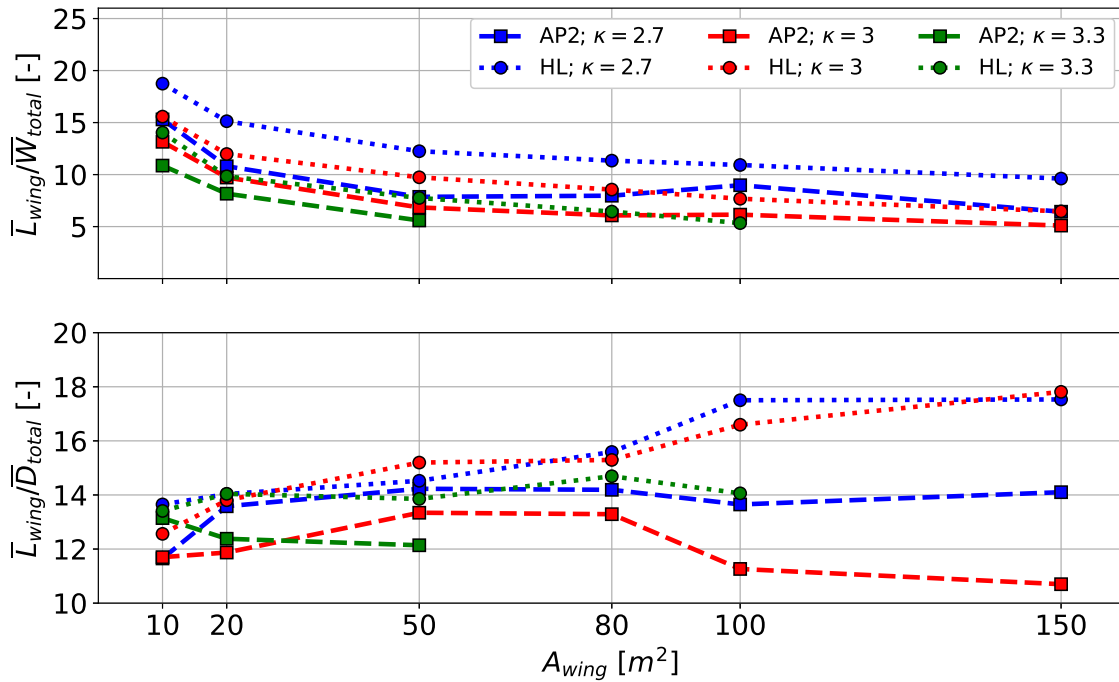
Figure 12. Load factor or lift $\overline{L}_{\mathrm{wing}}$ to $\overline{W}_{\mathrm{total}}$ ratio (top) and cycle-average total lift $\overline{L}_{\mathrm{wing}}$ to drag $\overline{D}_{\mathrm{total}}$, including tether drag, (bottom) during production phase (reel-out) for all aircraft sizes $A_{\mathrm{wing}} = 10 - 150 \,\mathrm{m}^2$, sets of aerodynamic coefficients AP2, HL and mass scaling exponents $\kappa = 2.7, \, 3, \, 3.3$ for wind data at the offshore location. Large-scale results for $A_{\mathrm{wing}} = 100, 150 \,\mathrm{m}^2$ might be misleading because only high wind speeds result in feasible solutions (compare figures 13).

diameter, assuming constant tensile tether strength. Tether length increases with AWES size and wind speed (see subsection 4.2) which further increases tether drag and weight.

Figure 14 compares the average power loss associated with tether drag $\overline{P}_{\mathrm{tether}}^{\mathrm{drag}}$, relative to average cycle power $\overline{P}$ for all
425   aircraft wing sizes $A_{\mathrm{wing}} = 10 - 150 \,\mathrm{m}^2$, mass scaling exponents $\kappa = 2.7, 3.0, 3.3$ and both sets of aerodynamic coefficients (HL, AP2). The relative tether drag loss decreases with wing area, because tether diameter scales beneficially with the square root of the tether force which scales linearly with wing area ($F_{\mathrm{tether}} \, sim A_{\mathrm{tether}} \sim d_{\mathrm{tether}}$).This scaling trend is encouraging, but counteracted and dominated by increasing tether and aircraft mass with wing area, highlighted in earlier sections. As expected, the high lift airfoil HL (dotted lines) experiences less relative drag loss than the AP2 reference airfoil (dashed lines),
430   due to higher average cycle power.
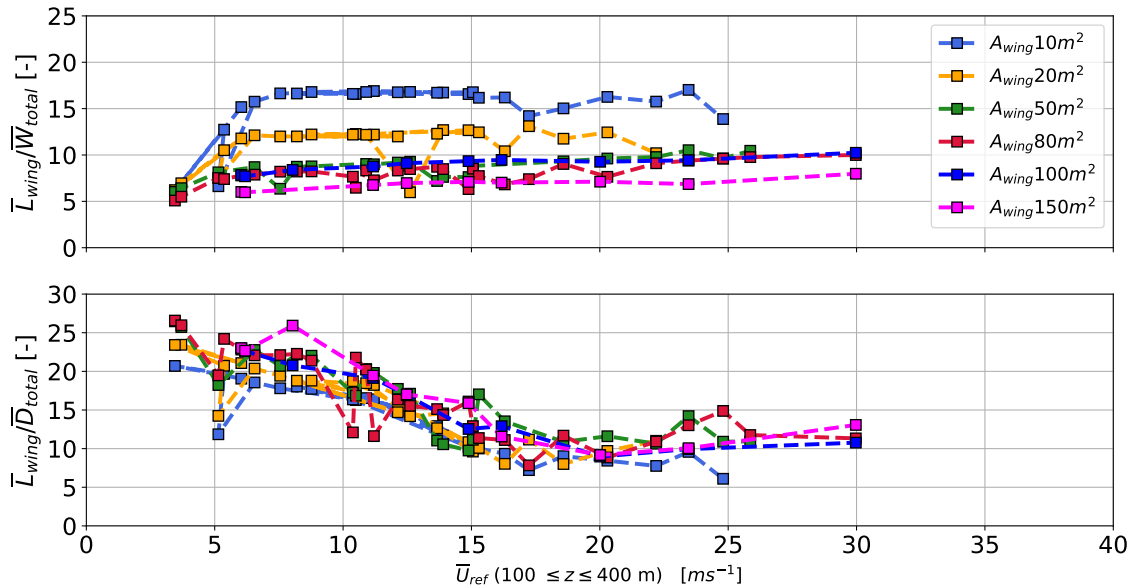
Figure 13. Ratio of cycle-average lift $\overline{L}_{\mathrm{wing}}$ to total weight $\overline{W}_{\mathrm{total}}$ (top), including tether weight, and cycle-average lift $\overline{L}_{\mathrm{wing}}$ to total drag $\overline{D}_{\mathrm{total}}$, including tether drag, (bottom) during production phase (reel-out) for all aircraft sizes $A_{\mathrm{wing}} = 10 - 150$ m^2 for AP2 reference aerodynamic coefficients and a mass scaling exponent of $\kappa = 2.7$ over reference wind speed at the offshore location.
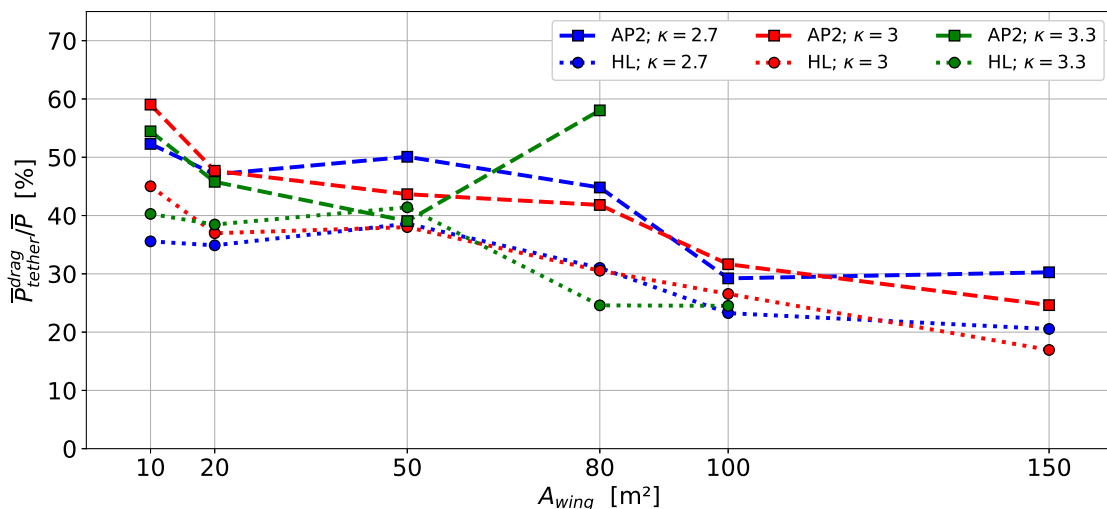
Figure 14. Ratio of cycle-average power losses due to tether drag $\overline{P}_{\mathrm{tether}}^{\mathrm{drag}}$ to avearge produced power $\overline{P}$ over aircraft size A_{wing} for both sets of aerodynamic coefficients AP2, HL, all mass scaling exponent of $\kappa = 2.7,\ 3.0,\ 3.3$ and wind data at the offshore location.

5 Summary and conclusion

This study presents AWES scaling trends and explores the AWES design space subject to representative onshore (Pritzwalk in northern Germany) and offshore (FINO3 research platform in the North Sea) wind conditions. We evaluate the impact of wing area and mass scaling as well as nonlinear aerodynamic properties on optimal trajectories, reaction forces and moments,

435   power generation and AEP, based on the `awebox` power and trajectory optimization model. Our analyses estimate a maximum average weight to average lift ratio (equivalent to a load factor of about 5) to allow viable AWES operation of about 20 %. Our results imply the existence of an upper limit of AWES weight relative to AWES size or lift, which is plausible since mass scales with aircraft volume and lift scales with aircraft area. In comparison, conventional WT power scales with the square and mass with the cube of the rotor diameter. Under the same assumptions AWES performance scales worse because the aircraft

440   needs to carry its own increasing weight, instead of being supported by a tower. Therefore, the optimal AWES size is always defined by the maximum weight which the aircraft can support, subject to local wind conditions.

In this work we described and analyzed ground-generation AWES scaling effects subject to realistic wind velocity profiles for a set of representative AWES. We compare the impact of several design parameters based on the Ampyx AP2 reference model. We analyze AWES performance for two sets of nonlinear aerodynamic coefficients, the AP2 reference and a wing with

445   high lift airfoil. To assess AWES scaling potential, several wing areas between $A_{\mathrm{wing}} = 10 - 150$ m, with mass properties scaled according to a geometric scaling law with three different mass scaling exponents $\kappa = 2.7,\ 3.0,\ 3.3$, were implemented into the `awebox` power and trajectory optimization toolbox. A representative set of k-means clustered onshore and offshore wind velocity profiles, derived from the mesoscale WRF model, were used to define wind inflow conditions.

We discussed the impact of mass and system size on typical trajectories and time series data which confirms that instan-

450   taneous power can drop to zero during the reel-out phase. This is caused by insufficient lift as the aircraft tries to overcome gravity and maintain tether tension. The minimum wind speed to sustain positive power production during the reel-out phase as well as tether length and average operating altitude increase with system size and weight. However, operating heights beyond 500 m are rare and mostly occur as the system de-powers above rated wind speed to stay within tether force and flight speed constraints. As these constraints become active, the resulting trajectory deforms and diverge from the expected paths seen for

455   lower wind speeds. This is especially true for high lift airfoils as they reach these limits faster. Since detailed design and stress analysis is beyond the scope of this paper, we limit ourselves to the estimation of maximum mechanical wing loads, assuming a elliptical lift distribution. Shear force scales linearly with wing area, while bending moment increases nonlinearly with wing area and wing span.

Analyzing the AWES power curve we determine that rated power scales linearly with wing area, assuming that tether speed

460   constraint are kept constant and the tether diameter is adjusted appropriately. We chose to size the tether diameter so that rated power is achieved at about $U_{\mathrm{ref}} = 10 \mathrm{ms}^{-1}$, independent of size, mass and location. A larger tether diameter would increase rated power and shift rated speed towards higher wind speeds, which might be beneficial for faster offshore wind conditions, but would impact tether drag and weight. Improving aerodynamic efficiency increases power production. For the sets of aerodynamic coefficients used in this study, average power increased by approximately 30% to 80 %, depending on

465 wing area. We proposed the nonlinear AWES power coefficient $c_\mathrm{p}^\mathrm{AWES} c_\mathrm{wing}^{-1}$ from the aircraft path length and wing area to collapse power curves.

We estimate AEP and cf based on the power curve analysis and wind speed probability distribution at reference height between $100 \leq z_\mathrm{ref} \leq 400\,\mathrm{m}$. Offshore AEP is generally higher than onshore, while the power curves are almost identical even though clustered profiles differ, due to higher wind speeds. Increased aircraft mass leads to significant reduction in AEP, as

470 lower wind speeds become infeasible to fly in until finally no feasible solutions, even at higher wind speeds, can be found. This is particularly true for the onshore location and AP2 reference aerodynamics, as these conditions do can not produce sufficient lift force to overcome system weight. Wind farm setups might therefore benefit from the deployment of multiple smaller AWES rather than few large-scale AWES. This could also reduce the overall power loss when synchronizing the flight trajectories of AWESs within a farm. Determining the ideal, site-specific AWES size needs to be determined subject to realistic mass scaling,

475 the available area and the local wind resource.

Furthermore, we describe the tether contribution to total weight and drag relative to aircraft wing size as well as tether-associated power losses. Our results show that even though relative tether power losses decrease with wing size, they still use up a significant portion (20 - 60 %) of the average mechanical AWES power.

Lastly, we try to determine the maximum AWES weight to lift ratio. Our data shows that total AWES weight, including

480 tether and aircraft, should not exceed 20 % of the produced aerodynamic lift to operate. The limitation of crosswind AWES operations seems to be the upward climb within each loop. During this ascent the aircraft decelerates by approximately 20%-25%, which reduces aerodynamic lift by about 35% - 45%, which could be offset by the deployment of additional high-lift devices. As a result the system can not produce enough lift to overcome gravity and maintain tether tension, leading to a reduction in tether speed and produced power up until a complete drop to zero for lower wind speeds.

485 # 6 Future work

Defining the AWES design space subject to realistic wind conditions and operating constraints is crucial for scaling this technology for large-scale deployment of grid-integration. We therefore propose to build upon this study and further investigate the design space using design optimization. A possible approach is to utilize the already existing AWES power and trajectory optimization toolbox `awebox` and implement it into a design optimization framework that varies parameters such as aspect

490 ratio, wing area and wing box dimensions. Adding a cost model would allow to optimize for levelized cost of electricity. Analyzing the dynamic aircraft wing loads caused by the cyclic nature of crosswind AWES and turbulence could improve AWES durability and further explore AWES design by considering fatigue loads to explore wing concepts to minimize κ. Ultimately, AWES must compete with conventional wind. Scaling and moving offshore are logical goals for both technologies. The relative merits of large-scale AWES must be further explored to set design and development targets, particularly since this

495 study highlighted that offshore AWES are not particularly beneficial relative to conventional wind, given the generally lower sheer offshore.

6.1 Acknowledgments and funding sources

The authors thank the BMWi for funding of the "OnKites I" and "OnKites II" project [grant number 0325394A] on the basis of a decision by the German Bundestag and project management Projektträger Jülich. We thank the PICS, NSERC and the DAAD for their funding.

`awebox` has been developed in collaboration with the company Kiteswarms Ltd. The company has also supported the `awebox` project through research funding. The `awebox` project has received funding from the European Union's Horizon 2020 research and innovation program under the Marie Sklodowska-Curie grant agreement No 642682 (AWESCO)

We thank the Carl von Ossietzky University of Oldenburg and the Energy Meteorology research group for providing access to their High Performance Computing cluster *EDDY* and ongoing support.

We further acknowledge Rachel Leuthold (University of Freiburg, SYSCOP) and Thilo Bronnenmeyer (Kiteswarms Ltd.) for their helped in writing this article, great, technical support and continued work on the `awebox`.

6.2 Author contributions

Markus Sommerfeld evaluated the data and wrote the manuscript in consultation and under the supervision of Curran Crawford. Martin Dörenkämper set up the numerical offshore simulation, contributed to the meteorological evaluation of the data and reviewed the manuscript. Jochem De Schutter co-developed the optimization model and helped writing and reviewed this manuscript.

Appendix A: figures
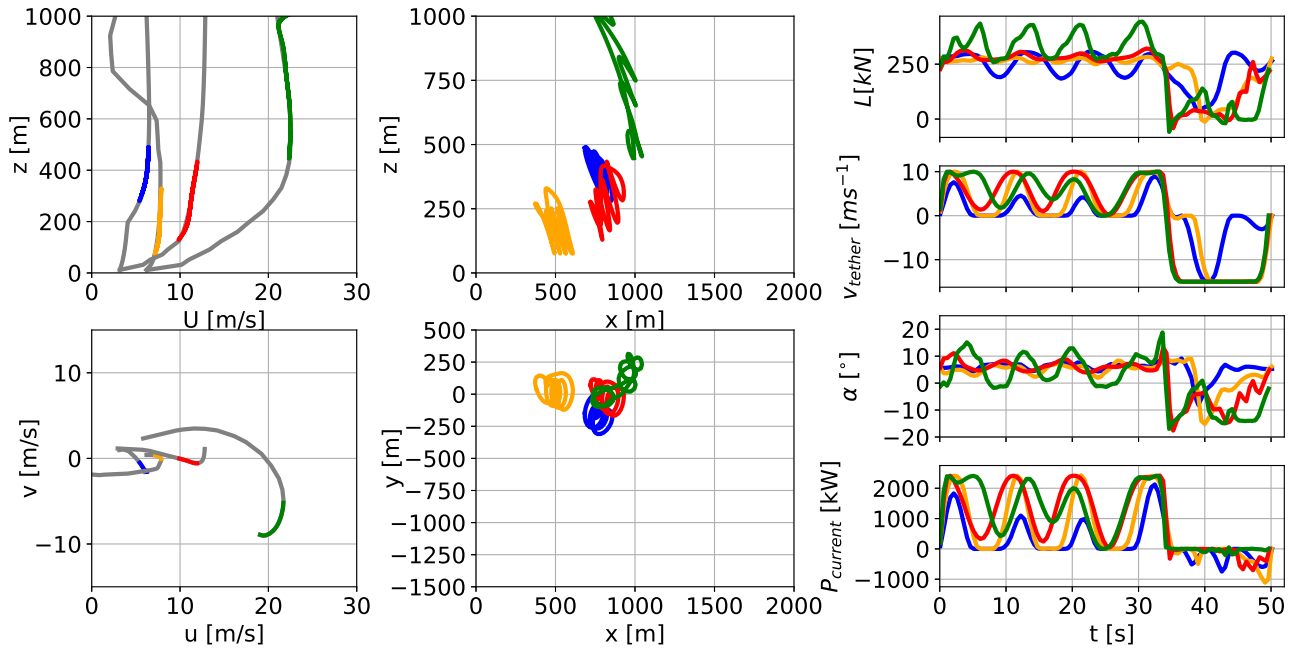
Figure A1. Optimal trajectory and time series for a ground-generation AWES with a wing area of $A_{\mathrm{wing}} = 50\ \mathrm{m}^2$, mass scaling exponent $\kappa = 3$ and HL aerodynamic coefficients. The left subfigures display representative onshore wind speed profiles (top), and hodograph of wind velocity up to 1000 m (bottom). The deviation of the colored lines is caused by the implementation of discrete WRF-simulated data points using Lagrange polynomials. Trajectories (center) in side and top view. The right subfigures show aerodynamic lift L, tether speed v_{tether}, angle of attack α and instantaneous power P_{current} time series, optimized subject to the corresponding wind velocity profiles.
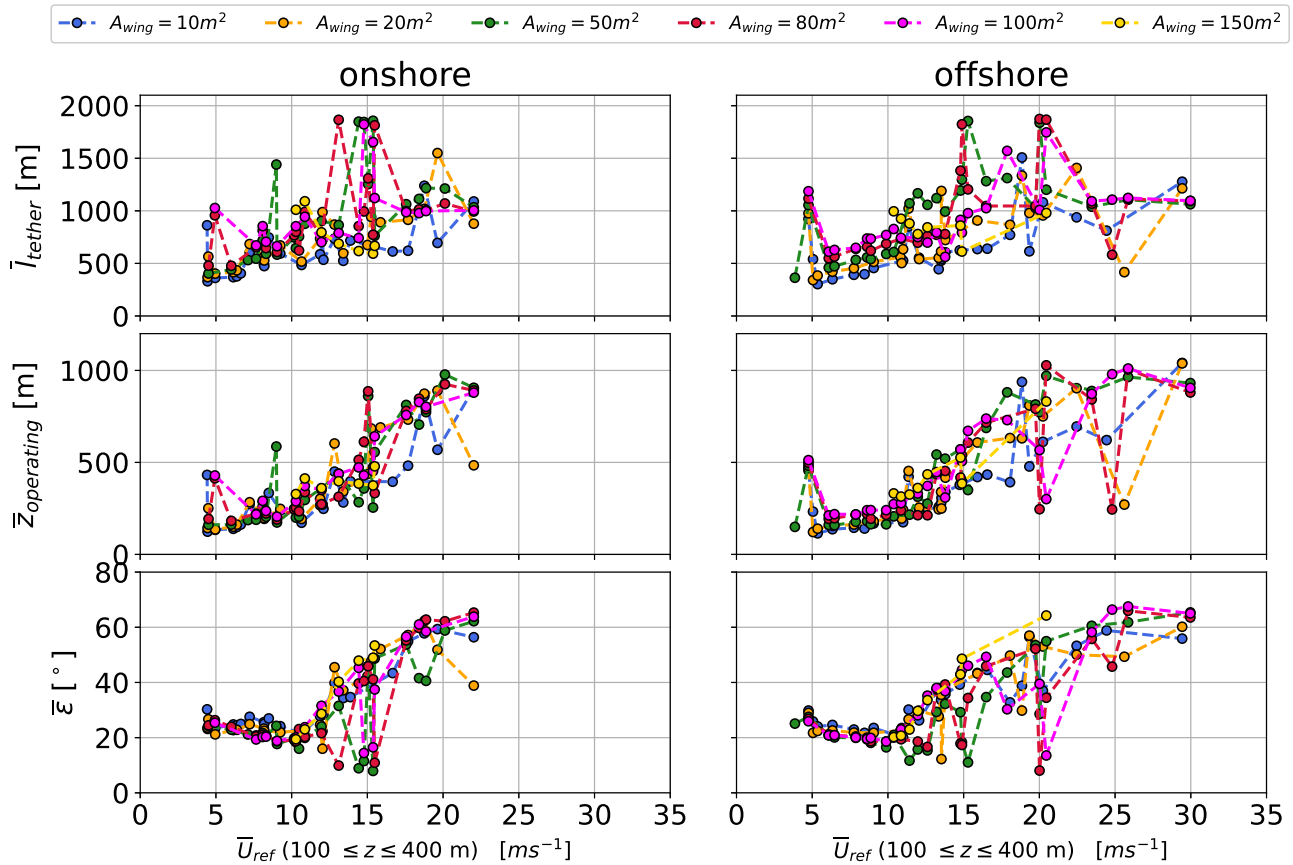
Figure A2. Average tether length $\bar{l}_{\text{tether}}$ (top), average operating altitude $\bar{z}_{\text{operating}}$ (center) and average elevation angle $\bar{\varepsilon}$ (bottom) over reference wind speed $\overline{U}_{\text{ref}}(100 \leq z \leq 400 \text{ m})$. Results for wing areas between $A_{\text{wing}} = 10 - 150 \text{ m}^2$ scaled with a mass scaling exponent of $\kappa = 3$, HL aerodynamic coefficients for both onshore (left) and offshore (right) location.
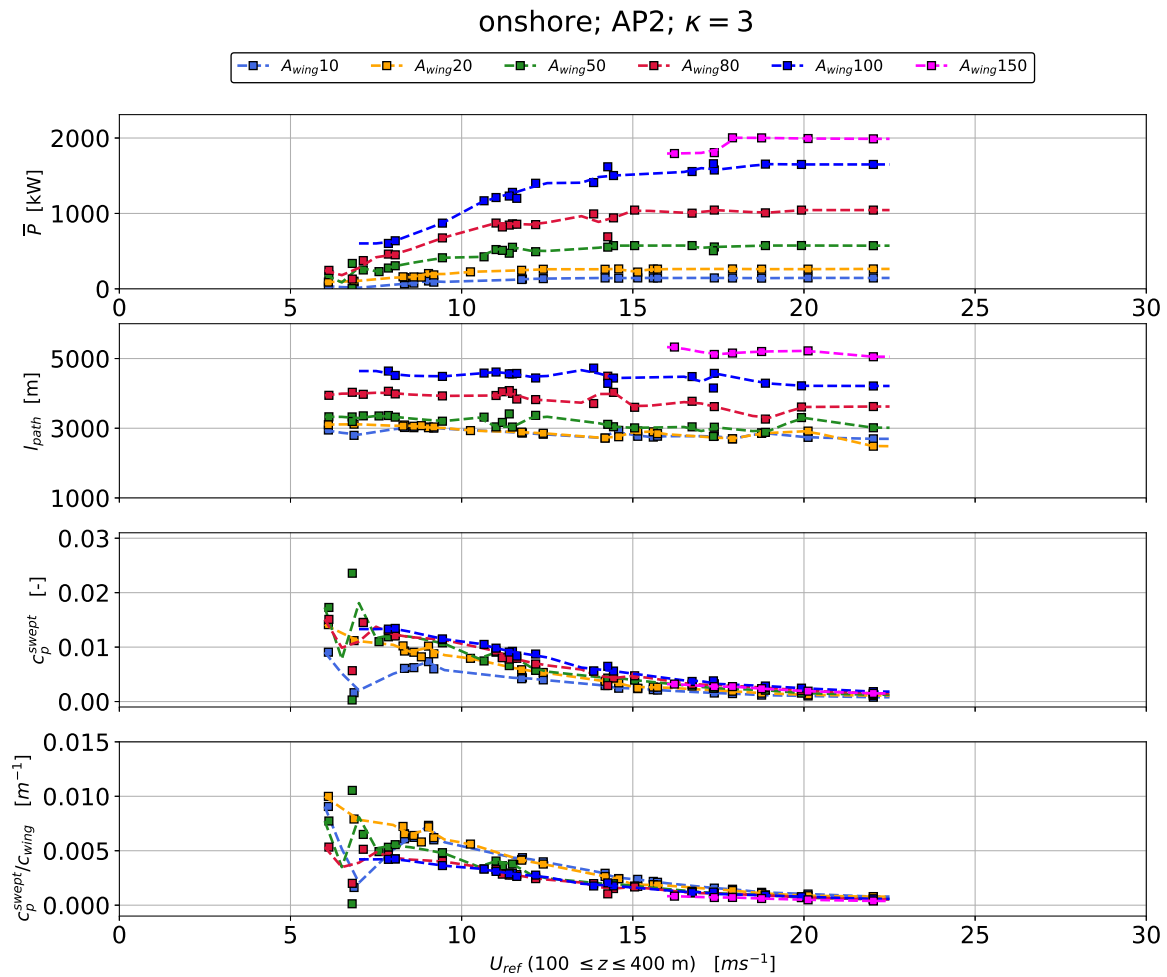
Figure A3. Power curve (top), path length (second from top), AWES power coefficient $c_{\mathrm{p}}^{\mathrm{AWES}}$ (third from top) and AWES power coefficient divided by chord length $c_{\mathrm{p}}^{\mathrm{AWES}}/c_{\mathrm{wing}}$ (bottom) over reference wind speed $100 \le z \le 400$ m scaled with $\kappa = 3.0$ for AWESs with $A_{\mathrm{wing}} = 10 - 150\,\mathrm{m}^2$ and AP2 reference aerodynamic coefficients. Data is derived from p5, p50, p95 wind velocity profiles within each of the k=10 onshore clusters. Missing data points are the result of infeasible combination of optimization constraints and boundary conditions.
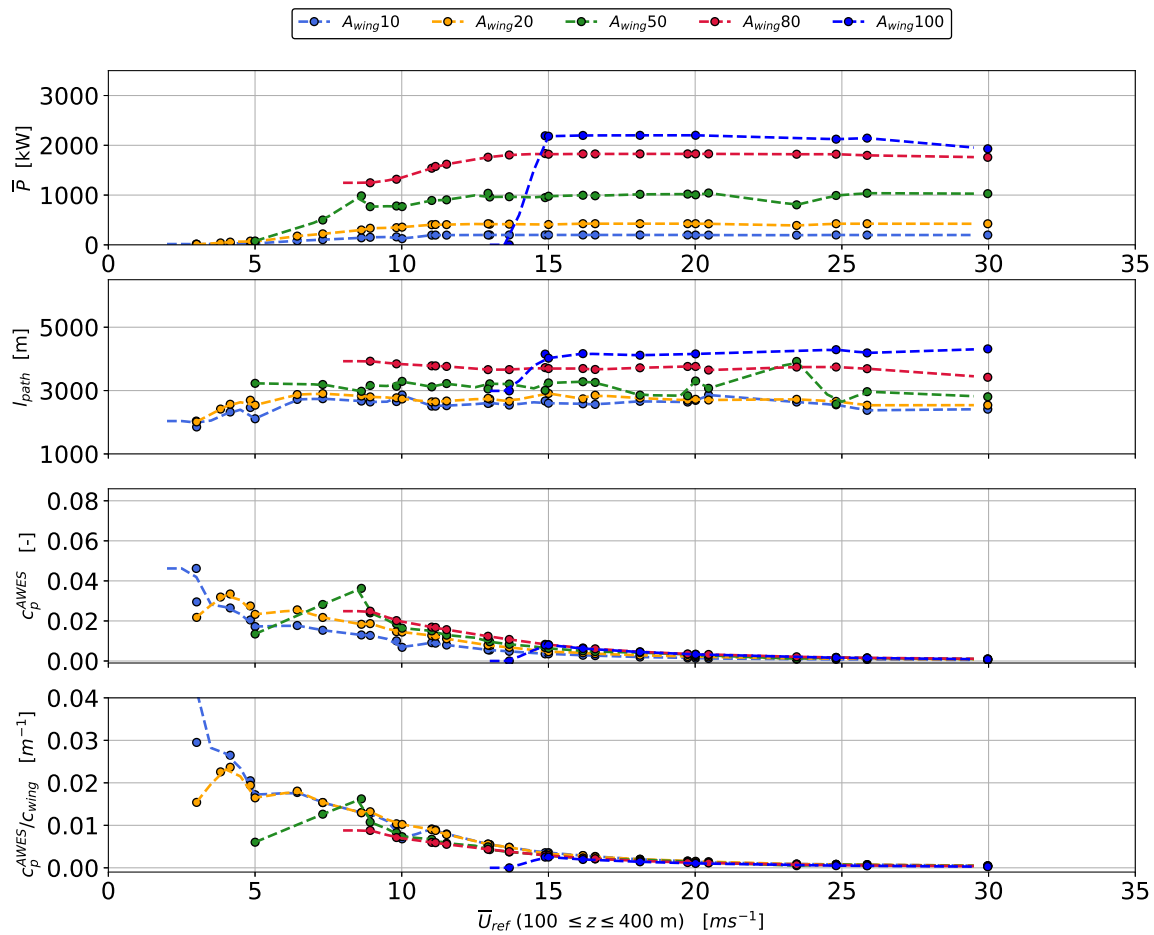
Figure A4. Power curve (top), path length (second from top), AWES power coefficient $c_\mathrm{p}^{\mathrm{AWES}}$ (third from top) and AWES power coefficient divided by chord length $c_\mathrm{p}^{\mathrm{AWES}}/c_{\mathrm{wing}}$ (bottom) over reference wind speed $100 \leq z \leq 400$ m for AWESs with $A_{\mathrm{wing}} = 10 - 150$ m^2 scaled with $\kappa = 3.3$ and HL aerodynamic coefficients. Data is derived from p5, p50, p95 wind velocity profiles within each of the k=10 offshore clusters. Missing data points are the result of infeasible combination of optimization constraints and boundary conditions.
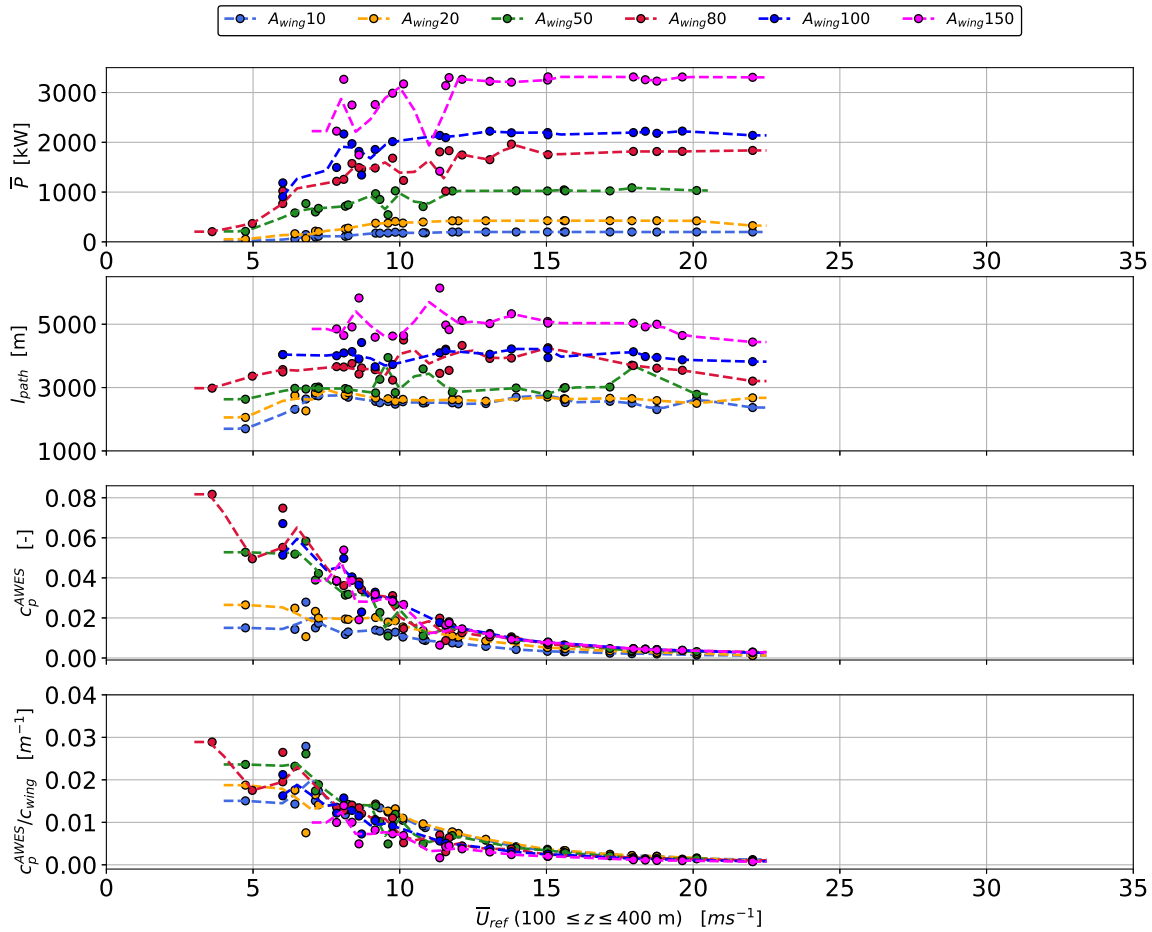
Figure A5. Power curve (top), path length (second from top), AWES power coefficient $c_\mathrm{p}^\mathrm{AWES}$ (third from top) and AWES power coefficient divided by chord length $c_\mathrm{p}^\mathrm{AWES}/c_\mathrm{wing}$ (bottom) over reference wind speed $100 \leq z \leq 400$ m for AWESs with $A_\mathrm{wing} = 10 - 150$ m^2 scaled with $\kappa = 2.7$ and HL aerodynamic coefficients. Data is derived from p5, p50, p95 wind velocity profiles within each of the k=10 offshore clusters. Missing data points are the result of infeasible combination of optimization constraints and boundary conditions.

References

515 Ampyx, .: Ampyx Power BV, https://www.ampyxpower.com/, last accessed: 2020-11-17.

Andersson, J., Åkesson, J., and Diehl, M.: CasADi: A Symbolic Package for Automatic Differentiation and Optimal Control, in: Recent Advances in Algorithmic Differentiation, edited by Forth, S., Hovland, P., Phipps, E., Utke, J., and Walther, A., pp. 297–307, Springer Berlin Heidelberg, Berlin, Heidelberg, 2012.

Bronnenmeyer, T.: Optimal Control for Multi-Kite Emergency Trajectories, Master's thesis, University of Stuttgart, https://cdn.syscop.de/
520 publications/Bronnenmeyer2018.pdf, last accessed: 2020-11-17, 2018.

De Schutter, J., Leuthold, R., Bronnenmeyer, T., Paelinck, R., and Diehl, M.: Optimal control of stacked multi-kite systems for utility-scale airborne wind energy, in: 2019 IEEE 58th Conference on Decision and Control (CDC), pp. 4865–4870, 2019.

Diehl, M.: Airborne Wind Energy: Basic Concepts and Physical Foundations, in: Airborne Wind Energy, edited by Ahrens, U., Diehl, M., and Schmehl, R., pp. 3–22, Springer Berlin Heidelberg, Berlin, Heidelberg, https://doi.org/10.1007/978-3-642-39965-7_1, 2013.

525 Dörenkämper, M., Olsen, B. T., Witha, B., Hahmann, A. N., Davis, N. N., Barcons, J., Ezber, Y., García-Bustamante, E., González-Rouco, J. F., Navarro, J., Sastre-Marugán, M., Sīle, T., Trei, W., Žagar, M., Badger, J., Gottschall, J., Sanz Rodrigo, J., and Mann, J.: The Making of the New European Wind Atlas – Part 2: Production and evaluation, Geoscientific Model Development, 13, 5079–5102, https://doi.org/10.5194/gmd-13-5079-2020, 2020.

Echeverri, P., Fricke, T., Homsy, G., and Tucker, N.: The Energy Kite - Selected Results From the Design, Development and Testing of
530 Makani's Airborne Wind Turbines - Part 1, Technical Report 1, Makani Power, https://storage.googleapis.com/x-prod.appspot.com/files/Makani_TheEnergyKiteReport_Part1.pdf, last accessed: 2020-11-17, 2020.

Ellis, G. and Ferraro, G.: The Social Acceptance of Wind Energy: Where we stand and the path ahead., Eur - scientific and technical research reports, European Commission, https://doi.org/10.2789/696070, 2016.

Federal Aviation Agency: Part 23 - Airworthiness Standards: Normal, Utility, Acrobatic, and Commuter Category Airplanes,
535 https://www.govinfo.gov/content/pkg/CFR-2017-title14-vol1/xml/CFR-2017-title14-vol1-part23.xml#seqnum23.337, last accessed: 2020-11-17, 2017.

Fingersh, L., Hand, M., and Laxson, A.: Wind Turbine Design Cost and Scaling Model, Tech. rep., U.S. Department of Energy, https://doi.org/10.2172/897434, 2006.

Gasch, R. and Twele, J.: Scaling wind turbines and rules of similarity, in: Wind Power Plants: Fundamentals, Design, Construction and
540 Operation, pp. 257–271, Springer Berlin Heidelberg, Berlin, Heidelberg, https://doi.org/10.1007/978-3-642-22938-1_7, 2012.

Gros, S., Zanon, M., and Diehl, M.: A relaxation strategy for the optimization of Airborne Wind Energy systems, in: 2013 European Control Conference (ECC), pp. 1011–1016, https://doi.org/10.23919/ECC.2013.6669670, 2013.

Haas, T., Schutter, J. D., Diehl, M., and Meyers, J.: Wake characteristics of pumping mode airborne wind energy systems, Journal of Physics: Conference Series, 1256, 012 016, https://doi.org/10.1088/1742-6596/1256/1/012016, 2019.

545 Horn, G., Gros, S., and Diehl, M.: Numerical Trajectory Optimization for Airborne Wind Energy Systems Described by High Fidelity Aircraft Models, pp. 205–218, Springer Berlin Heidelberg, Berlin, Heidelberg, https://doi.org/10.1007/978-3-642-39965-7_11, 2013.

HSL: The HSL Mathematical Software Library, http://www.hsl.rl.ac.uk/, last accessed: 2020-06-14.

Leuthold, R., De Schutter, J., Malz, E. C., Licitra, G., Gros, S., and Diehl, M.: Operational Regions of a Multi-Kite AWE System, in: 2018 European Control Conference (ECC), pp. 52–57, https://doi.org/10.23919/ECC.2018.8550199, 2018.

550 Leuthold, R., De Schutter, J., Malz, E., Licitra, G., Bronnenmeyer, T., Gros, S., and Diehl, M.: awebox: Modelling and optimal control of single- and multiple-kite systems for airborne wind energy, https://github.com/awebox, 2020.

Loyd, M. L.: Crosswind kite power (for large-scale wind power production), Journal of Energy, 4, 106–111, https://doi.org/10.2514/3.48021, 1980.

Luchsinger, R. H.: Pumping Cycle Kite Power, pp. 47–64, Springer Berlin Heidelberg, Berlin, Heidelberg, https://doi.org/10.1007/978-3-642-39965-7_3, 2013.

555

Lunney, E., Ban, M., Duic, N., and Foley, A.: A state-of-the-art review and feasibility analysis of high altitude wind power in Northern Ireland, Renewable and Sustainable Energy Reviews, 68, 899 – 911, https://doi.org/10.1016/j.rser.2016.08.014, 2017.

Makani: Makani Technologies LLC, https://x.company/projects/makani/, last accessed: 2020-06-14.

Malz, E., Koenemann, J., Sieberling, S., and Gros, S.: A reference model for airborne wind energy systems for optimization and control, Renewable Energy, 140, 1004 – 1011, https://doi.org/10.1016/j.renene.2019.03.111, 2019.

560

Malz, E., Verendel, V., and Gros, S.: Computing the power profiles for an Airborne Wind Energy system based on large-scale wind data, Renewable Energy, 162, 766 – 778, https://doi.org/10.1016/j.renene.2020.06.056, 2020.

Malz, E. C., Zanon, M., and Gros, S.: A Quantification of the Performance Loss of Power Averaging in Airborne Wind Energy Farms, in: 2018 European Control Conference (ECC), pp. 58–63, 2018.

565 Pedregosa, F., Varoquaux, G., Gramfort, A., Michel, V., Thirion, B., Grisel, O., Blondel, M., Prettenhofer, P., Weiss, R., Dubourg, V., Vanderplas, J., Passos, A., Cournapeau, D., Brucher, M., Perrot, M., and Duchesnay, E.: Scikit-learn: Machine Learning in Python, Journal of Machine Learning Research, 12, 2825–2830, 2011.

Salvação, N. and Guedes Soares, C.: Wind resource assessment offshore the Atlantic Iberian coast with the WRF model, Energy, 145, 276 – 287, https://doi.org/10.1016/j.energy.2017.12.101, 2018.

570 Sommerfeld, M.: Power curve characterization for ground-generation AWES, Wind Energy Science, submitted Nov 2020, 2020.

Sommerfeld, M., Crawford, C., Monahan, A., and Bastigkeit, I.: LiDAR-based characterization of mid-altitude wind conditions for airborne wind energy systems, Wind Energy, 22, 1101–1120, https://doi.org/10.1002/we.2343, 2019a.

Sommerfeld, M., Dörenkämper, M., Steinfeld, G., and Crawford, C.: Improving mesoscale wind speed forecasts using lidar-based observation nudging for airborne wind energy systems, Wind Energy Science, 4, 563–580, https://doi.org/10.5194/wes-4-563-2019, 2019b.

575 Stull, R. B.: An Introduction to Boundary Layer Meteorology, vol. 13, Springer Science & Business Media, https://doi.org/10.1007/978-94-009-3027-8, 2012.

Torenbeek, E. and Wittenberg, H.: Flight Physics: Essentials of Aeronautical Disciplines and Technology, with Historical Notes, Springer Netherlands, https://doi.org/10.1007/978-1-4020-8664-9, 2009.

Wächter, A. and Biegler, L. T.: On the implementation of an interior-point filter line-search algorithm for large-scale nonlinear programming,

580 Mathematical Programming, 106, 25–57, https://doi.org/10.1007/s10107-004-0559-y, 2006.